Reconfigurable Intelligent Surfaces: A signal processing perspective with wireless applications

Citation for the original published paper (version of record):
Björnson, E., Wymeersch, H., Matthiesen, B. et al (2022). Reconfigurable Intelligent Surfaces: A signal processing perspective with wireless applications. IEEE Signal Processing Magazine, 39(2): 135-158. http://dx.doi.org/10.1109/MSP.2021.3130549

Emil Björnson, Henk Wymeersch, Bho Matthiesen, Petar Popovski,
Luca Sanguinetti, and Elisabeth de Carvalho

Reconfigurable Intelligent Surfaces


SHUTTERSTOCK.COM/SDECORET

A signal processing perspective with wireless applications

Antenna array technology enables the directional transmission and reception of wireless signals for communication, localization, and sensing purposes. The signal processing algorithms that underpin it began to be developed several decades ago [1], but it was with the deployment of 5G wireless mobile networks that the technology became mainstream [2]. The number of antenna elements in the arrays of 5G base stations (BSs) and user devices can be measured on the order of hundreds and tens, respectively. As networks shift toward using higher-frequency bands, more antennas fit into a given aperture. For communication purposes, the arrays are harnessed to form beams in desired directions to improve the signal-to-noise ratio (SNR) and multiplex data signals in the spatial domain (to one or multiple devices) and to suppress interference by spatial filtering [2]. For localization purposes, these arrays are employed to maintain the SNR when operating across wider bandwidths, for angle-of-arrival estimation, and to separate multiple sources and scatterers [3]. The practical use of these features requires that each antenna array is equipped with well-designed signal processing algorithms.

Digital Object Identifier 10.1109/MSP.2021.3130549
Date of current version: 24 February 2022

1053-5888/22©2022IEEE

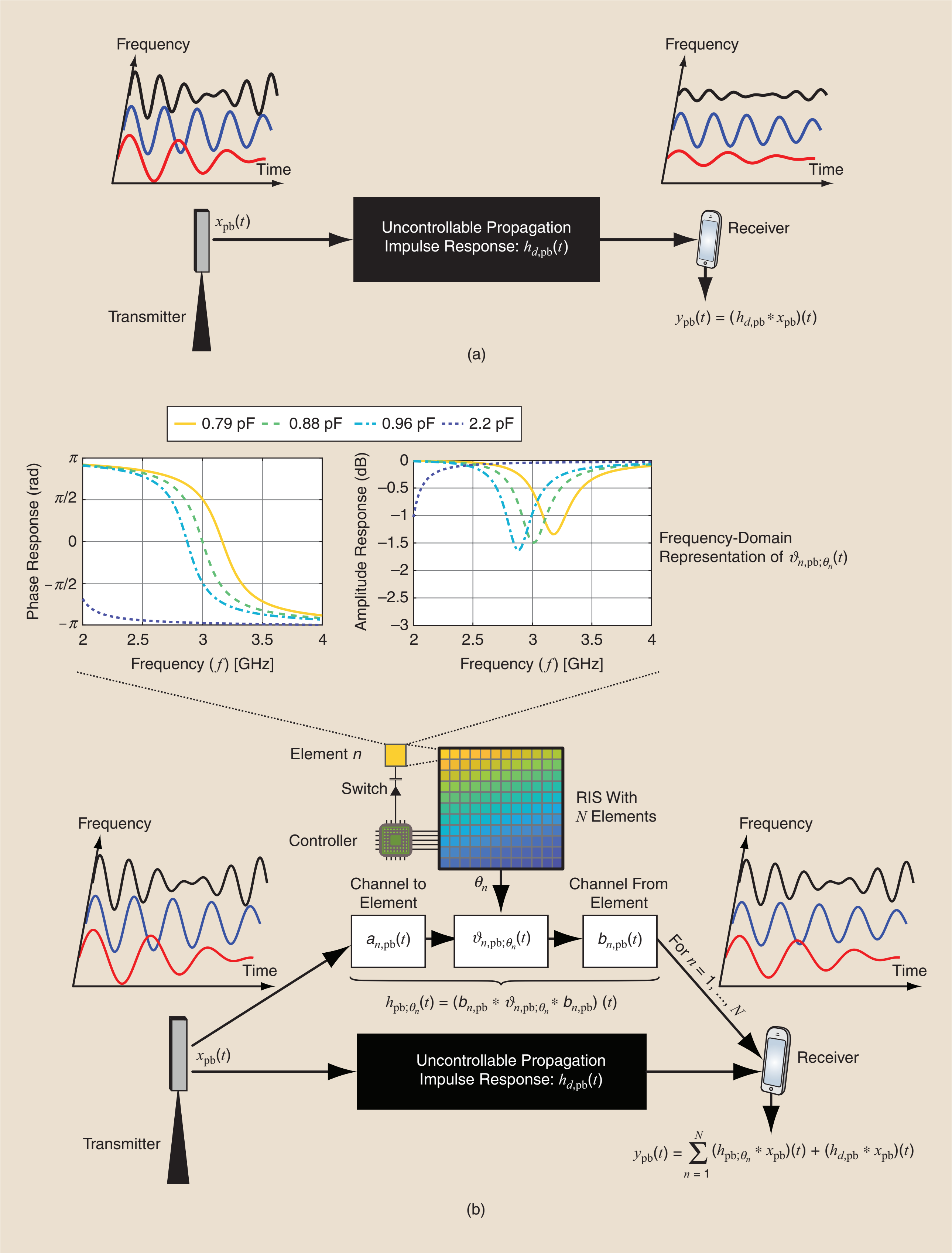

FIGURE 1. The propagation channel in current wireless systems is uncontrollable. When an RIS with N elements is added to the system, N controllable paths are added to the end-to-end channel. The amplitude and phase of each element can be tuned to improve the signal quality at the receiver. (a) A conventional wireless system where the channel propagation is uncontrollable. (b) An RIS-aided communication system with controllable propagation paths.

5G developments enhance transmitter and receiver functionalities, but wireless channel propagation remains an uncontrollable system. This is illustrated in Figure 1(a), and its mathematical notation will be introduced later. Transmitted signals with three different frequencies are shown to demonstrate the fact that attenuation can vary greatly across frequencies. Looking beyond 5G, the advent of electromagnetic components that can shape how they interact with wireless signals enables partial control of propagation. A reconfigurable intelligent surface (RIS) is a 2D surface of engineered material whose properties are reconfigurable rather than static [4]. As detailed in Figure 1(b), the surface consists of an array of discrete elements, where each color represents a certain amplitude and phase response curve. A controller and switch determine which curve to utilize on a per-element or group-of-elements level. The scattering, absorption, reflection, and diffraction properties of the entire RIS can thereby be changed with time and controlled by software.

In principle, the surface can be used to synthesize an arbitrarily shaped object of the same size, when it comes to how electromagnetic waves interact with it [5]. Figure 1(b) describes how the RIS adds new controllable paths to complement the uncontrollable propagation, each containing a wireless channel to an RIS element, filtering inside the element, and a wireless channel to the receiver. These paths can be tuned to improve the channel quality in a variety of ways [6]. For example, Figure 1(a) shows how the uncontrollable channel attenuates some signal frequencies more than others, while Figure 1(b) relates how the RIS can be tuned to mitigate this issue. An RIS can be utilized to support wireless communications as well as localization, sensing, and wireless power transfer [7], [8].

The long-term vision for RIS technology is to create smart radio environments [9], where wireless propagation conditions are co-engineered with physical-layer signaling, and investigate how to utilize this new capability. The traditional protocol stack consists of seven layers, and wireless technology is chiefly focused on the first three (physical, link, and network) [10]. Conventional design starts at layer 1, where the physical signals are generated and radiated by the transmitter and then measured and decoded by the receiver. The wireless medium between the transmitter and receiver, layer 0, is commonly seen as uncontrollable and decided by "nature." RIS technology changes this by extending the protocol design to layer 0, which can profoundly alter wireless systems beyond 5G.

This article provides a tutorial on the fundamental properties of the RIS technology from a signal processing perspective. It is meant as a complement to recent surveys of electromagnetic and hardware aspects [4], [7], [11], acoustics [12], communication theory [13], and localization [8]. We provide the formulas and derivations that are required to understand and analyze RIS-aided systems using signal processing and exemplify how they can be employed for improved communication, localization, and sensing. We also elaborate on the fundamentally new possibilities enabled by layer 0 engineering and phenomena that remain to be modeled and utilized for improved signal processing design. The simulation examples can be reproduced using code available at https://github.com/emilbjornson/SPM_RIS.

History and fundamentals

RIS is an umbrella term that recently appeared in the communication domain [14], but the technology has deep roots in the electromagnetic field [4], [11], [15], [16]. There are several decades of research on how to build such surfaces and control their properties as well as implementation concepts using different materials for various frequencies and use cases. The common feature is that the surfaces consist of many discrete elements with controllable properties, which are illustrated as colored squares in Figure 1(b). The elements are passive circuits in the sense that incoming signals are reradiated after filtering that cannot increase the power. Each element filters a signal by potentially reducing the amplitude, incurring delays, and changing the polarization. Each element performs this filtering passively based on its local impedance, but the key feature of an RIS is that the impedance can be reconfigured through time by external stimuli.

Figure 1(b) exemplifies how each element is connected by a switch (e.g., a varactor) to a programmable controller that can tune the impedance of the element, thereby controlling the reflection coefficient that determines the change in amplitude and phase of the reradiated signal [17]. The elements are typically subwavelength in size (e.g., a square patch of size $\lambda/5 \times \lambda/5$) to behave as scatterers without strong intrinsic directivity [18]. An RIS can then receive signals from any direction from the half space toward which its elements are facing and tune the pattern of reflection coefficients across the elements to reradiate signals with the desired direction and beam shape. We will explain the signal processing algorithms that enable this type of operation in the following.

RIS technology appears under different names, such as software-controlled metasurfaces [6], intelligent reflecting surfaces [19], and a few others [2]. It should be viewed as a general concept for creating smart radio environments in which the exact hardware characteristics have been abstracted away. However, it is likely that metasurfaces, where the elements are made of thin layers of metamaterial, will play a major role in practical implementations. Metamaterials have recently been successfully utilized for commercial antenna design in terrestrial and satellite communications (e.g., by Pivotal Commware and Kymeta) as well as radar (e.g., by Echodyne). RIS technology is different in the sense that the surface is not colocated with the transmitter or the receiver of the wireless signals but deployed in between, which opens the door for a variety of new use cases as well as novel signal processing challenges regarding how to exploit the ability to partially control the channel. The new electromagnetic properties of RIS-aided systems require changes in the established models for discrete signal processing used in communication and localization and create the need to reexamine the classical system models from first principles to ensure that the technology builds on a solid foundation. The objective of this article is to provide such a basis.

End-to-end system modeling

The uncontrollable propagation channel in Figure 1(a) is a system that can be analyzed using classical signal processing methods. However, the controllable paths in Figure 1(b) have unusual properties that we will shed light on by providing the connection between the continuous-time representations of channels and hardware and the corresponding discrete-time models needed for digital signal processing.

Consider a single-antenna transmitter that sends a wireless passband signal $x_{\mathrm{pb}}(t)$, with time variable $t \in \mathbb{R}$, to a receiver via an RIS consisting of N scattering elements. We begin by considering the entire system as uncontrollable; more precisely, it is modeled as linear and time invariant (LTI) with the real-valued impulse response $h_{\mathrm{pb}}(t)$. It then follows from standard signal processing theory that the output signal $y_{\mathrm{pb}}(t)$ is the convolution between the input and impulse response:

$$y_{\mathrm{pb}}(t) = (h_{\mathrm{pb}} * x_{\mathrm{pb}})(t) = \int_{-\infty}^{\infty} h_{\mathrm{pb}}(u) x_{\mathrm{pb}}(t-u)\,du. \tag{1}$$

The characterizing feature of an RIS is that its properties can change with time. Hence, this LTI model can be utilized only for the duration of one configuration with a fixed impulse response $h_{\mathrm{pb}}(t)$. We can distinguish between two RIS regimes: 1) piecewise constant, in which $h_{\mathrm{pb}}(t)$ does not change while the signal of interest is nonzero and 2) continuously varying, for which the LTI model in (1) is not valid. This tutorial focuses on the former category, where the LTI model can be used for the duration of one configuration, but we will briefly describe the second class when discussing mobility effects.

Suppose the transmitted signal is generated from a complex-valued baseband signal $x(t)$ with bandwidth $B/2$ that is modulated to the carrier frequency f_c, which satisfies $B \leq 2f_c$ and usually $B \ll f_c$. For example, a typical scenario in 5G is $f_c = 3\,\mathrm{GHz}$ and $B = 100\,\mathrm{MHz}$. The transmitted passband signal will then have bandwidth B and can be expressed as

$$x_{\mathrm{pb}}(t) = \Re\left(\sqrt{2}\,x(t)e^{j2\pi f_c t}\right) = \frac{x(t)e^{j2\pi f_c t} + x^*(t)e^{-j2\pi f_c t}}{\sqrt{2}}, \tag{2}$$

where $\Re(\cdot)$ outputs the real part of its argument, $j = \sqrt{-1}$ is the imaginary unit, and $\sqrt{2}$ keeps the power constant. If we let $\mathcal{F}_c\{\cdot\}$ denote the continuous Fourier transform, the relation in (2) is equivalent to

$$X_{\mathrm{pb}}(f) = \frac{X(f-f_c) + X^*(-f-f_c)}{\sqrt{2}}, \tag{3}$$

where $X_{\mathrm{pb}}(f) = \mathcal{F}_c\{x_{\mathrm{pb}}(t)\}$ and $X(f) = \mathcal{F}_c\{x(t)\}$ are the frequency-domain representations of the passband and baseband signals, respectively. The frequency response $H_{\mathrm{pb}}(f) = \mathcal{F}_c\{h_{\mathrm{pb}}(t)\}$ describes how the system filters different signal frequencies, generally changing the amplitude and delay differently.

When analyzing passband systems in communication and localization, it is convenient to abstract away the carrier frequency and consider only the baseband signal $x(t)$, which, by definition, has the same power as $x_{\mathrm{pb}}(t)$. We then need to find the baseband counterpart to the input–output relation in (1). Many textbooks derive such a relation for the special case of $h_{\mathrm{pb}}(t)$ being a band-limited passband filter, but we cannot make that assumption since our system describes a wireless propagation environment that can handle input signals with arbitrary frequency content. Hence, we will briefly present the so-called complex pseudobaseband representation, where the received signal $y(t)$ is defined via $y_{\mathrm{pb}}(t) = \Re(\sqrt{2}\,y(t)e^{j2\pi f_c t})$. By taking the Fourier transform of both sides of (1) and utilizing (3), we obtain

$$\begin{aligned} Y_{\mathrm{pb}}(f) &= H_{\mathrm{pb}}(f)\frac{X(f-f_c) + X^*(-f-f_c)}{\sqrt{2}} \\ &= \frac{\overbrace{H_{\mathrm{pb}}(f)X(f-f_c)}^{Y(f-f_c)} + \overbrace{H^*_{\mathrm{pb}}(-f)X^*(-f-f_c)}^{Y^*(-f-f_c)}}{\sqrt{2}}, \end{aligned} \tag{4}$$

where we use the notation $Y_{\mathrm{pb}}(f) = \mathcal{F}_c\{y_{\mathrm{pb}}(t)\} = (Y(f-f_c) + Y^*(-f-f_c))/\sqrt{2}$ and $Y(f) = \mathcal{F}_c\{y(t)\}$. The final equality utilizes the property $H_{\mathrm{pb}}(f) = H^*_{\mathrm{pb}}(-f)$ for real-valued systems. From (4), we can identify the Fourier transform of the received baseband signal as

$$Y(f-f_c) = H_{\mathrm{pb}}(f)X(f-f_c) \;\Rightarrow\; Y(f) = H_{\mathrm{pb}}(f+f_c)X(f). \tag{5}$$

Taking the inverse Fourier transform of (5) yields

$$y(t) = (h * x)(t) = \int_{-\infty}^{\infty} h(u)x(t-u)\,du, \tag{6}$$

where the impulse response $h(t) = h_{\mathrm{pb}}(t)e^{-j2\pi f_c t}$ is the complex pseudobaseband representation of the system. The adjective *pseudo* indicates that the downshifted $h(t)$ is not a baseband filter, but the output signal $y(t)$ is baseband anyway since we input the baseband signal $x(t)$. The key benefits of the pseudobaseband representation are that we can vary the bandwidth B of $x_{\mathrm{pb}}(t)$ without changing the impulse response and that $h(t)$ represents the true physical system instead of a baseband-filtered version of it.

Continuous-time system model with RIS elements as reconfigurable filters

The signal $x_{\mathrm{pb}}(t)$ is the transmitted electromagnetic signal in Figure 1(b), and $y_{\mathrm{pb}}(t)$ is the filtered version that reaches the receiver. We now describe how the impulse responses of the RIS paths in Figure 1(b) can be modeled in the pseudobaseband. For brevity, we consider only the controllable channel via the RIS in this section. We will later enrich the model by including the uncontrollable part, which can describe a line-of-sight (LOS) path and scattered paths not involving the RIS. We characterize the impulse response $h_{\mathrm{pb};\boldsymbol{\theta}}(t)$ of the end-to-end channel filter, and we add the subscript $\boldsymbol{\theta} = [\theta_1, \ldots, \theta_N]^{\mathrm{T}}$ to indicate that the impulse response is configured by a set of external control variables $\theta_1,\ldots,\theta_N$ that will be defined in the following. For each of the N scattering elements of the RIS, the transmitted signal $x_{\mathrm{pb}}(t)$ will propagate to it across an LTI channel represented by an arbitrary impulse response $a_{n,\mathrm{pb}}(t)$ for element $n = 1,\ldots,N$. If its frequency response has a constant amplitude and linear phase across the passband used by the signal, we call it a *narrowband channel*. We otherwise term it a *wideband channel*.

When the signal reaches element n, it will be filtered inside n and then reradiated. It all happens in the analog domain, and we consider a passive operation that can be described by an LTI filter. The special RIS feature is that the impulse response $\vartheta_{n,\mathrm{pb};\theta_n}(t)$ is reconfigurable in the sense that it is determined by an external stimulus represented by the variable θ_n. Depending on the RIS implementation, this control variable can take values in discrete and continuous sets. To be consistent with the LTI assumption, only one value can be utilized during the considered signal transmission, and it is selected before the transmission is initiated. Since the element is much smaller than the wavelength, it can be modeled as a passive electric circuit. The passiveness implies there is no added noise within the circuit [7]. In principle, one can also build an RIS with active circuit components (e.g., to make the operation dependent on the content of the impinging signal), but this will inevitably add noise and will not be covered in this tutorial.

The upper part of Figure 1(b) shows the frequency response for the element implementation considered in [20]. The intended carrier frequency is $f_c = 3$ GHz, and since the frequency response (i.e., the reflection coefficient) is complex, we show the phase and amplitude responses around the carrier. Each configuration results in one curve and is achieved by tuning the impedance. In this example, it is tuned by varying the capacitance via a varactor, but other implementations use PIN diodes, microelectromechanical systems, and optical mechanisms [4], [11]. The phase response is shown for four different capacitance values, which have been selected to give the phase shifts $\pi/2, 0, -\pi/2, \pi$ at the carrier frequency. There are large phase variations across the gigahertz range, created by the linear phase shift that a constant time delay would produce and nonlinearity created by the frequency-dependent impedance of the element. However, we can neglect the latter effect if the signal bandwidth B is limited to a few tens of megahertz.

The frequency responses of wireless channels typically vary as fast or faster than the frequency response of the RIS element does with frequency; thus, it is usually these channels that determine whether the end-to-end channel $h(t)$ is narrow- or wideband. The phase shifts are caused by three phenomena. The example curves begin close to $+\pi$ because the reradiated electric field is inverted. As f increases, a constant time delay leads to a larger phase shift. The amplitude response is also provided in Figure 1(b) and reveals that the amplitude loss depends on the frequency and capacitance. The losses are largest when tuning the RIS to achieve zero phase response due to resonance in the circuit. However, a few decibels of signal loss in the RIS element is a minor issue compared to propagation losses across wireless channels that can be on the order of 100 dB.

The signal that is reradiated from element n propagates to the receiver across an LTI channel with an arbitrary impulse response $b_{n,\mathrm{pb}}(t)$. Since the transmitted signal propagates via element n across a cascade of three LTI filters, the joint impulse response is the convolution of their impulse responses: $(b_{n,\mathrm{pb}} * \vartheta_{n,\mathrm{pb};\theta_n} * a_{n,\mathrm{pb}})(t)$. This happens for all the N elements; thus, we obtain the input–output relation

$$\begin{aligned} y_{\mathrm{pb}}(t) &= \sum_{n=1}^{N} (b_{n,\mathrm{pb}} * \vartheta_{n,\mathrm{pb};\theta_n} * a_{n,\mathrm{pb}} * x_{\mathrm{pb}})(t) \\ &= \Bigg(\underbrace{\left[\sum_{n=1}^{N} b_{n,\mathrm{pb}} * \vartheta_{n,\mathrm{pb};\theta_n} * a_{n,\mathrm{pb}}\right]}_{=h_{\mathrm{pb};\boldsymbol{\theta}}} * x_{\mathrm{pb}}\Bigg)(t), \end{aligned} \tag{7}$$

where we identify $h_{\mathrm{pb};\boldsymbol{\theta}}(t) = \sum_{n=1}^{N}(b_{n,\mathrm{pb}} * \vartheta_{n,\mathrm{pb};\theta_n} * a_{n,\mathrm{pb}})(t)$ as the impulse response of the end-to-end system. Recall from (6) that filtering in the passband can be transformed into pseudobaseband filtering by downshifting the filters. By applying this principle to each filter in $h_{\mathrm{pb};\boldsymbol{\theta}}(t)$, we obtain the complex pseudobaseband representation

$$y(t) = \sum_{n=1}^{N} (b_n * \vartheta_{n;\theta_n} * a_n * x)(t), \tag{8}$$

where $a_n(t) = a_{n,\mathrm{pb}}(t)e^{-j2\pi f_c t}$, $b_n(t) = b_{n,\mathrm{pb}}(t)e^{-j2\pi f_c t}$, and $\vartheta_{n;\theta_n}(t) = \vartheta_{n,\mathrm{pb};\theta_n}(t)e^{-j2\pi f_c t}$ are the channels and filter associated with element n. The end-to-end channel has impulse response $h_{\boldsymbol{\theta}}(t) = \sum_{n=1}^{N}(b_n * \vartheta_{n;\theta_n} * a_n)(t)$. The fact that the convolution between a chain of impulse responses in the passband becomes a convolution between the corresponding chain of pseudobaseband impulse responses is a unique feature of the complex pseudobaseband representation that we consider. The conventional textbook formulation, where each filter is assumed to be passband, gives rise to extra scaling factors.

Equivalent discrete-time system model

The continuous-time complex baseband signal $x(t)$ is usually generated to represent a complex discrete-time signal $x[m]$, where m is the integer time index, via pulse-amplitude modulation (PAM). We consider ideal PAM using a unit energy sinc pulse $p(t) = \sqrt{B}\,\mathrm{sinc}(Bt)$ and the symbol rate B, for which

$$x(t) = \sum_{m=-\infty}^{\infty} x[m]\,p\Big(t - \frac{m}{B}\Big). \tag{9}$$

Since the actual input signal $x[m]$ is in discrete time, it is convenient to abstract away the entire continuous-time description by sampling the received signal to obtain an end-to-end discrete-time system model. Before sampling, we must add the thermal receiver noise and low-pass filtering at the receiver into the model. We model the noise by a white, circularly symmetric, complex Gaussian random process $w(t)$ with power-spectral density N_0. Adding it to the received signal in (6) as $z(t) = y(t) + w(t)$, we obtain

$$z(t) = (h_{\boldsymbol{\theta}} * x)(t) + w(t) = \sum_{m=-\infty}^{\infty} x[m](h_{\boldsymbol{\theta}} * p)\left(t - \frac{m}{B}\right) + w(t), \tag{10}$$

where the equality follows from (9).

Since the desired signal is band limited to $|f| \leq B/2$, while the noise is not, we filter $z(t)$ using an ideal low-pass filter with impulse response $p(t)$, the same as in (9), to remove the out-of-band noise. We then take samples at the symbol rate at time instants $t = k/B + \eta$, where k is the integer sample index and η is the sampling delay at the receiver, to obtain

$$z[k] = (p * z)(t)\big|_{t=k/B+\eta} = \sum_{m=-\infty}^{\infty} x[m] h_{\boldsymbol{\theta}}[k-m] + w[k], \tag{11}$$

where the discrete-time impulse response is defined as

$$\begin{aligned} h_{\boldsymbol{\theta}}[k] &= (p * h_{\boldsymbol{\theta}} * p)(t)\big|_{t=k/B+\eta} \\ &= \sum_{n=1}^{N} (p * b_n * \vartheta_{n;\theta_n} * a_n * p)(t)\Bigg|_{t=k/B+\eta} \end{aligned} \tag{12}$$

by inserting the RIS system model from (8). Note that the discrete-time impulse response is created by low-pass filtering the end-to-end continuous-time impulse response $h_{\boldsymbol{\theta}}(t)$ and then taking samples of it. The discrete-time noise $w[k]$ in (11) is circularly symmetric complex Gaussian distributed since $w(t)$ is Gaussian and independent for different k since $(p * w)(t)$ has $\operatorname{sinc}(B(t_1 - t_2))$ as autocorrelation:

$$w[k] = (p * w)(t)\big|_{t=k/B+\eta} \sim \mathcal{N}_{\mathbb{C}}(0, N_0). \tag{13}$$

The discrete-time model in (11) applies to any system but can be simplified by considering the specific properties that wireless channels and practical signals and systems possess: 1) the channels are causal and incur a finite maximum delay, 2) the ideal sinc pulse $p(t)$ is approximated by a time-limited Nyquist pulse (i.e., requiring a bandwidth slightly larger than B, where B is the symbol rate), 3) the sampling delay η is selected to obtain a causal discrete-time system. This implies that the channel is a finite-impulse response (FIR) filter with $M \geq 1$ terms:

$$\begin{aligned} z[k] &= \sum_{m=k-M+1}^{k} x[m] h_{\boldsymbol{\theta}}[k-m] + w[k] \\ &= \sum_{\ell=0}^{M-1} h_{\boldsymbol{\theta}}[\ell] x[k-\ell] + w[k], \end{aligned} \tag{14}$$

where $h_{\boldsymbol{\theta}}[0], \dots, h_{\boldsymbol{\theta}}[M-1]$ are the nonzero components of the impulse response.

Canonical multicarrier system model

The discrete-time system model in (14) describes a dispersive channel with a memory of $M-1$ previous symbols; that is, the received $z[k]$ contains not only the currently transmitted signal $x[k]$ but also intersymbol interference from $x[k-1], \dots, x[k-M+1]$. A common way to untangle the interference is to design the transmitted symbols by using orthogonal frequency-division multiplexing (OFDM), transforming the channel into a collection of separate frequency subcarriers. We provide the corresponding reformulated system model, which will be utilized for communication and localization.

Suppose we want to transmit a block of K symbols, $\chi[0], \dots, \chi[K-1]$, and append a so-called cyclic prefix to obtain the following sequence of length $K + M - 1$ that can be transmitted over the input-output system defined in (14):

$$x[k] = \begin{cases} \chi[k] & k = 0, \dots, K-1 \\ \chi[k+K] & k = -M+1, \dots, -1. \end{cases} \tag{15}$$

Since we added the final $M-1$ symbols as a prefix, we can interpret (14) as a cyclic convolution between $\{\chi[k] : k = 0, \dots, K-1\}$ and $\{h_{\boldsymbol{\theta}}[k] : k = 0, \dots, M-1\}$, plus noise if $K > M$. Let us define the K-point discrete Fourier transform (DFT) of an arbitrary sequence $s[k]$ as $\mathcal{F}_d\{s[k]\} = \left(1/\sqrt{K}\right) \sum_{k=0}^{K-1} s[k] e^{-j2\pi k\nu/K}$, where the scaling factor keeps the energy constant. Taking the DFT of (14) and given the fact that cyclic convolution becomes the product of the corresponding Fourier transforms, we obtain the K orthogonal subcarriers

$$\bar{z}[\nu] = \bar{h}_{\boldsymbol{\theta}}[\nu] \bar{x}[\nu] + \bar{w}[\nu], \quad \nu = 0, \dots, K-1, \tag{16}$$

where $\bar{z}[\nu] = \mathcal{F}_d\{z[k]\}$ and $\bar{x}[\nu] = \mathcal{F}_d\{x[k]\}$ describe the received and transmitted signals, respectively, in the frequency domain.

At subcarrier ν, the frequency response of the end-to-end channel is

$$\bar{h}_{\boldsymbol{\theta}}[\nu] = \sum_{k=0}^{M-1} h_{\boldsymbol{\theta}}[k] e^{-j2\pi k\nu/K}, \tag{17}$$

and the transformed noise $\bar{w}[\nu] = \mathcal{F}_d\{w[k]\} \sim \mathcal{N}_{\mathbb{C}}(0, N_0)$ is independent for $\nu = 0, \dots, K-1$. Notice that (16) has a more convenient structure than (14) since there is no intersymbol interference. It is known as a *discrete memoryless channel with additive white Gaussian noise* (*AWGN*). OFDM exploits this feature by treating $\bar{x}[\nu]$ as the transmitted signal and $\bar{z}[\nu]$ as the received signal. In an OFDM implementation, the transmitted time domain $x[k]$ is generated from $\bar{x}[\nu]$ by an inverse Fourier transform, while the receiver computes the Fourier transform of its received signal $z[k]$ to obtain $\bar{z}[\nu]$.

Example of multipath channels

We now give a concrete example of how the end-to-end channel $\bar{h}_{\boldsymbol{\theta}}[\nu]$ in the OFDM system model (16) is determined by the propagation channels and RIS elements. Suppose the channel from the transmitter to the nth RIS element consists of L_a propagation paths; then, the impulse response is modeled as

$$\begin{aligned} a_{n,\mathrm{pb}}(t) &= \sum_{l=1}^{L_a} \sqrt{\alpha_n^l}\,\delta(t-\tau_{n,a}^l) \\ \Rightarrow \quad a_n(t) &= \sum_{l=1}^{L_a} \sqrt{\alpha_n^l}\,e^{-j2\pi f_c t}\delta(t-\tau_{n,a}^l), \end{aligned} \tag{18}$$

where $\alpha_n^l \in [0,1]$ is the propagation loss and $\tau_{n,a}^l \geq 0$ is the delay of the lth path, while $\delta(t)$ denotes the Dirac delta function. Similarly, suppose there are L_b propagation paths from the nth RIS element to the receiver; then, the impulse response can be modeled as

$$\begin{aligned} b_{n,\mathrm{pb}}(t) &= \sum_{\ell=1}^{L_b} \sqrt{\beta_n^\ell}\,\delta(t-\tau_{n,b}^\ell) \\ \Rightarrow \quad b_n(t) &= \sum_{\ell=1}^{L_b} \sqrt{\beta_n^\ell}\,e^{-j2\pi f_c t}\delta(t-\tau_{n,b}^\ell), \end{aligned} \tag{19}$$

where $\beta_n^\ell \in [0,1]$ is the propagation loss and $\tau_{n,b}^\ell \geq 0$ is the delay of the ℓth path. We assume that the signal bandwidth is sufficiently small to make the frequency response of the RIS element constant in amplitude and time delay (i.e., linear phase); that is, the RIS is narrowband while the wireless channels might be wideband. For a given configuration $\theta_n \in \Omega$ selected from some set Ω of feasible configurations, element n is reradiating a fraction $\gamma_{\theta_n} \in [0,1]$ of the incident signal power and incurs a delay of $\tau_{\theta_n} \geq 0$ so that

$$\begin{aligned} \vartheta_{n,\mathrm{pb};\theta_n}(t) &= \sqrt{\gamma_{\theta_n}}\,\delta(t-\tau_{\theta_n}) \\ \Rightarrow \quad \vartheta_{n;\theta_n}(t) &= \sqrt{\gamma_{\theta_n}}\,e^{-j2\pi f_c t}\delta(t-\tau_{\theta_n}). \end{aligned} \tag{20}$$

Under these assumptions, the discrete-time impulse response in (12) particularizes to

$$\begin{aligned} h_{\boldsymbol{\theta}}[k] = \sum_{n=1}^{N}\sum_{l=1}^{L_a}\sum_{\ell=1}^{L_b} \sqrt{\alpha_n^l\beta_n^\ell\gamma_{\theta_n}}\,e^{-j2\pi f_c(\tau_{n,a}^l+\tau_{n,b}^\ell+\tau_{\theta_n})} \\ \cdot \underbrace{\mathrm{sinc}\,(k+B(\eta-\tau_{n,a}^l-\tau_{n,b}^\ell-\tau_{\theta_n}))}_{\approx\,\mathrm{sinc}(k+B(\eta-\tau_{n,a}^l-\tau_{n,b}^\ell))}, \end{aligned} \tag{21}$$

where the approximation utilizes the fact that the delay in the RIS is much smaller than the propagation delays, so its impact on the symbol rate is negligible: $B\tau_{\theta_n} \approx 0$. However, since $f_c \gg B$, the RIS creates phase shifts $2\pi f_c \tau_{\theta_n}$ in (21) that are substantial (within a few periods of 2π), as represented in Figure 1(b). We notice from (21) that there are NL_aL_b paths from the transmitter to the receiver, each having a unique propagation loss $\alpha_n^l\beta_n^\ell\gamma_{\theta_n}$, which is the product of the losses between the transmitter to an RIS element, losses inside the element, and losses from the element to the receiver. Due to the product operation, each path is very weak, but the large number of paths can potentially lead to a good SNR. Each path is also associated with a phase shift $e^{-j2\pi f_c(\tau_{n,a}^l+\tau_{n,b}^\ell+\tau_{\theta_n})}$ containing the accumulated delays. The sinc function determines how the signal energy carried by the path is divided between the M taps of the FIR filter.

The frequency response $\bar{h}_{\boldsymbol{\theta}}[\nu]$ can now be computed using (17). To obtain a compact expression, we first notice that (21) can be expressed as an inner product of two vectors:

$$\begin{aligned} &h_{\boldsymbol{\theta}}[k] = \\ &\underbrace{\begin{bmatrix} \sum_{l=1}^{L_a}\sum_{\ell=1}^{L_b} \sqrt{\alpha_1^l\beta_1^\ell}\,e^{-j2\pi f_c(\tau_{1,a}^l+\tau_{1,b}^\ell)}\mathrm{sinc}\,(k+B(\eta-\tau_{1,a}^l-\tau_{1,b}^\ell)) \\ \vdots \\ \sum_{l=1}^{L_a}\sum_{\ell=1}^{L_b} \sqrt{\alpha_N^l\beta_N^\ell}\,e^{-j2\pi f_c(\tau_{N,a}^l+\tau_{N,b}^\ell)}\mathrm{sinc}\,(k+B(\eta-\tau_{N,a}^l-\tau_{N,b}^\ell)) \end{bmatrix}^{\mathrm{T}}}_{\boldsymbol{v}_k^{\mathrm{T}}} \\ &\cdot \underbrace{\begin{bmatrix} \sqrt{\gamma_{\theta_1}}\,e^{-j2\pi f_c\tau_{\theta_1}} \\ \vdots \\ \sqrt{\gamma_{\theta_N}}\,e^{-j2\pi f_c\tau_{\theta_N}} \end{bmatrix}}_{\boldsymbol{\omega}_{\boldsymbol{\theta}}}. \end{aligned} \tag{22}$$

The propagation channels determine $\boldsymbol{v}_k \in \mathbb{C}^N$, while the RIS determines $\boldsymbol{\omega}_{\boldsymbol{\theta}} \in \mathbb{C}^N$ and is the same for all k. Hence, $\boldsymbol{v}_k$ is given by nature, while $\boldsymbol{\omega}_{\boldsymbol{\theta}}$ is controllable. We can compute the frequency response as

$$\underbrace{\begin{bmatrix} \bar{h}_{\boldsymbol{\theta}}[0] \\ \vdots \\ \bar{h}_{\boldsymbol{\theta}}[K-1] \end{bmatrix}}_{\bar{\boldsymbol{h}}_{\boldsymbol{\theta}}} = \boldsymbol{F}\underbrace{\begin{bmatrix} h_{\boldsymbol{\theta}}[0] \\ \vdots \\ h_{\boldsymbol{\theta}}[M-1] \end{bmatrix}}_{\boldsymbol{h}} = \boldsymbol{F}\boldsymbol{V}^{\mathrm{T}}\boldsymbol{\omega}_{\boldsymbol{\theta}}, \tag{23}$$

where $\boldsymbol{V} = [\boldsymbol{v}_0, \ldots, \boldsymbol{v}_{M-1}]$ is an $N \times M$ matrix and $\boldsymbol{F}$ is a $K \times M$ DFT matrix with the (ν,k)th element being $e^{-j2\pi k\nu/K}$. We make use of this notation when considering wideband systems.

Simplified narrowband system model

When there is only one strong path to and from the RIS (i.e., the LOS path), we can select the sampling delay η to make $B(\eta-\tau_{n,a}^l-\tau_{n,b}^\ell)=0$ for that path. By setting $L_a = L_b = 1$ and omitting the superscripts indicating the path indices, we can rewrite the impulse response in (21) as

$$\begin{aligned} h_{\boldsymbol{\theta}}[k] &= \sum_{n=1}^{N} \sqrt{\alpha_n\beta_n\gamma_{\theta_n}}\,e^{-j2\pi f_c(\tau_{n,a}+\tau_{n,b}+\tau_{\theta_n})}\mathrm{sinc}(k) \\ &= \begin{cases} \sum_{n=1}^{N} \sqrt{\alpha_n\beta_n\gamma_{\theta_n}}\,e^{-j2\pi f_c(\tau_{n,a}+\tau_{n,b}+\tau_{\theta_n})} & k=0 \\ 0 & k \neq 0. \end{cases} \end{aligned} \tag{24}$$

A channel of this kind is called narrowband and the input–output system in (11) simplifies to

$$\begin{aligned} z[k] &= h_{\boldsymbol{\theta}}[0]x[k] + w[k] \\ &= \sum_{n=1}^{N} \sqrt{\alpha_n\beta_n\gamma_{\theta_n}}\,e^{-j2\pi f_c(\tau_{n,a}+\tau_{n,b}+\tau_{\theta_n})}x[k] + w[k]. \end{aligned} \tag{25}$$

This is a popular special case where there is no need for OFDM since there is no intersymbol interference. The model can also be derived when there are multiple paths with a delay spread much smaller than the sampling period $1/B$, making them indistinguishable. In the LOS case, we can relate the channel coefficients to the steering vector $\boldsymbol{a}(\boldsymbol{\phi}) \in \mathbb{C}^N$ of the RIS, which describes the phase shift pattern across the elements when a plane wave arrives from the azimuth/elevation angle pair $\boldsymbol{\phi} \in \mathbb{R}^2$. The RIS geometry determines the steering vector, and a general way to compute it is found in [21]. Using the steering vector, we can write $\Sigma_{n=1}^{N} \sqrt{\alpha_n \beta_n \gamma_{\theta_n}}\, e^{-j2\pi f_c(\tau_{n,a}+\tau_{n,b}+\tau_{\theta_n})} = \sqrt{\alpha\beta}\, e^{j\psi_{\mathrm{RIS}}}(\boldsymbol{a}(\boldsymbol{\phi}_a) \odot \boldsymbol{a}(\boldsymbol{\phi}_b))^{\mathrm{T}} \boldsymbol{\omega}_{\boldsymbol{\theta}}$, where $\alpha = \alpha_n$, $\beta = \beta_n$ for all n, ψ_{RIS} is a common phase shift, $\boldsymbol{\phi}_a$ is the angle to the transmitter, and $\boldsymbol{\phi}_b$ is the angle to the receiver. We use this geometric modeling for simulations and localization.

RIS-aided communication

The central element when characterizing the performance of a communication channel is the probabilistic relation between the discrete-time input x and output z, specified by the conditional probability density function $p(z|x)$. For example, the narrowband system in (25) has the complex symbols x and z as inputs and outputs, respectively. The received signal for the kth transmitted symbol is

$$z[k] = h_{\boldsymbol{\theta}} x[k] + w[k], \quad k = 0, 1, \ldots, \tag{26}$$

where a discrete sequence $\{x[k]\}$ of code word symbols describing the payload data is transmitted and each one is attenuated by a factor $h_{\boldsymbol{\theta}} \in \mathbb{C}$ and corrupted by the independent noise $w[k] \sim \mathcal{N}_{\mathbb{C}}(0, N_0)$.

To arrive at the well-known communication model of an AWGN channel, we need some further assumptions. First, $h_{\boldsymbol{\theta}}$ is fixed for all symbols in a given code word, and its value is known to the transmitter and receiver. Second, we assume that the power limit of the sender is P Watt. Since there are B symbols per second, each symbol should satisfy the power constraint $\mathbb{E}\{|x[k]|^2\} \leq P/B$. Finally, the transmitter must know the SNR of the channel, which is given by $\mathsf{SNR} = P|h_{\boldsymbol{\theta}}|^2/(BN_0)$. The capacity of this AWGN channel is

$$C = B\log_2(1 + \mathsf{SNR}) = B\log_2\left(1 + \frac{P|h_{\boldsymbol{\theta}}|^2}{BN_0}\right) \ \text{bit/s}. \tag{27}$$

If any of the preceding assumptions are violated (e.g., $h_{\boldsymbol{\theta}}$ is not known by the receiver or the SNR is not known by the transmitter), the channel is not AWGN, and the capacity formula (27) is not valid. For a deeper discussion of how assumptions affect the definition of a communication channel, see [10, Ch. 6].

This discussion can be extrapolated to the OFDM channel in (16), obtained as a superposition of K parallel memoryless AWGN channels. In this case, we need to consider a set of K channel values $\{\bar{h}_{\boldsymbol{\theta}}[\nu]\}$, each associated with one of the narrowband subcarrier channels. Given the transmitter, the receiver, and a narrowband channel, an obvious objective of an RIS would be to select the configuration $\boldsymbol{\theta}$ to create a channel $h_{\boldsymbol{\theta}}$ that maximizes the capacity (27). More generally, in case of OFDM, the objective is to create a set of K channels $\{\bar{h}_{\boldsymbol{\theta}}[\nu]\}$ that maximizes the sum of the capacity of the constituent subcarrier channels. In this case, the values of the channels $\bar{h}_{\boldsymbol{\theta}}[0], \ldots, \bar{h}_{\boldsymbol{\theta}}[K-1]$ may not be independently optimized, as they are determined by the same RIS configuration.

To have the RIS configured, it is necessary that it is capable of receiving control information from the radio infrastructure. There are two principal types of channels for sending this information: out-of-band and in-band. An out-of-band control channel does not consume part of the useful bandwidth B and is implemented as a wired link or wireless channel that uses different frequency spectrum. The RIS-controlled channel in (26) implicitly assumes that the control information has been exchanged through an out-of-band channel before the actual communication starts.

In contrast, an in-band control channel consumes part of the useful bandwidth to configure the RIS, and this should be factored in when computing the overall capacity of the wireless channel. The in-band control information can be sent before the actual communication. However, it is also possible to have an in-band control channel in which the RIS control information is simultaneously sent with the payload data. In this case, the RIS should be able to decode the control information embedded in $x[k]$ and, based on that, causally change the value of $h_{\boldsymbol{\theta}}$ (i.e., change $\boldsymbol{\theta}$) for symbols with indices $j > k$. It is immediately clear that the end-to-end channel cannot be an AWGN channel anymore. In an information-theoretic sense, this situation corresponds to a relay channel in which the source broadcasts two types of data: payload (intended for the receiver) and control (intended for the RIS that becomes a relay node). Based on the received data, the RIS changes the configuration of the end-to-end channel.

The authors of [5], [22], and [23] compare RIS-aided and traditional relay-aided systems. Here, we provide a different perspective by using the layering framework, as depicted in Figure 2. We consider a wireless connection between node 1 and node 2, aided by a cascade of RISs and relays. Nodes 1 and 2 implement all protocol layers (not depicted). Suppose node 1 transmits to node 2. The wireless signal is reflected by RIS 1, which is configured using an out-of-band control channel. The payload data (the blue line) stay at layer 0 (the wireless medium), meaning that the RIS affects only the propagation environment, without processing the communication flow. The control information (the red line) shows that there needs to be an out-of-band communication between node 1, node 2, and RIS 1 to select a suitable configuration $\boldsymbol{\theta}$.

Next, the signal reaches RIS 2, which uses an in-band control channel. The payload data stay at layer 0, while the RIS controller decodes the control information and adapts its configuration. Then, the signal reaches a nonregenerative amplify-and-forward relay. The payload data go through layer 1 (physical), where the signal is amplified and the active circuitry introduces additional noise. The depicted control channel is out-of-band, but, similar to the RIS 1 case, it can be implemented in-band, using a dedicated communication protocol that is not employed by the payload data. Finally, the decode-and-forward relay decodes the payload and control data and is capable of interpreting the control information.

RIS design for narrowband capacity maximization

To explain how an RIS can be used to maximize capacity, we begin by considering a simple setup: a single-antenna transmitter communicates with a single-antenna receiver across a narrowband channel. We further assume that the RIS elements can be perfectly configured: we can select $\tau_{\theta_n} \geq 0$ so that $2\pi f_c \tau_{\theta_n}$ can take any value between zero and 2π for $n = 1, \ldots, N$, while the amplitude response is constant $\gamma_{\boldsymbol{\theta}_n} = \gamma$. The considered system is a memoryless AWGN channel with $h_{\boldsymbol{\theta}} = \Sigma_{n=1}^{N} \sqrt{\alpha_n \beta_n \gamma}\, e^{-j2\pi f_c(\tau_{n,a} + \tau_{n,b} + \tau_{\theta n})}$; thus, the capacity in (27) becomes $B \log_2(1 + \mathrm{SNR})$, with

$$\begin{aligned} \mathrm{SNR} &= \frac{P}{BN_0} \left| \sum_{n=1}^{N} \sqrt{\alpha_n \beta_n \gamma}\, e^{-\mathrm{j}2\pi f_c(\tau_{n,a} + \tau_{n,b} + \tau_{\theta n})} \right|^2 \\ &= \frac{P}{BN_0} \left| \begin{bmatrix} \sqrt[4]{\alpha_1 \beta_1 \gamma} \\ \vdots \\ \sqrt[4]{\alpha_N \beta_N \gamma} \end{bmatrix}^{\mathrm{T}} \begin{bmatrix} e^{-\mathrm{j}2\pi f_c(\tau_{1,a} + \tau_{1,b} + \tau_{\theta 1})} \sqrt[4]{\alpha_1 \beta_1 \gamma} \\ \vdots \\ e^{-\mathrm{j}2\pi f_c(\tau_{N,a} + \tau_{N,b} + \tau_{\theta N})} \sqrt[4]{\alpha_N \beta_N \gamma} \end{bmatrix} \right|^2, \quad (28) \\ &\leq \frac{P}{BN_0} \left| \sum_{n=1}^{N} \sqrt{\alpha_n \beta_n \gamma} \right|^2, \quad (29) \end{aligned}$$

where the final step follows from the Cauchy–Schwartz inequality.

The upper bound in that inequality is achieved if and only if the two vectors in (28) are parallel, which occurs when $e^{-j2\pi f_c(\tau_{n,a} + \tau_{n,b} + \tau_{\theta n})}$ is the same for all n [24]. Hence, each RIS element should phase shift its reradiated signal so that it reaches the receiver synchronously in phase with the signals from all the other RIS elements. There are multiple solutions due to the phase periodicity, but the one causing the minimum overall time delay is [25]

$$\tau_{\theta_n} = \left(\max_{i=1,\ldots,N} \tau_{i,a} + \tau_{i,b} \right) - \tau_{n,a} - \tau_{n,b}, \quad (30)$$

where $\tau_{\theta_n} = 0$ for the element experiencing the largest propagation delay while all other elements add positive delays $\tau_{\theta_n} > 0$ to match the largest propagation delay.

Suppose all N paths have the same propagation loss: $\alpha_n \beta_n = \alpha\beta$. This is a common property when the RIS is in the far field of the transmitter and receiver. It then follows that $|\Sigma_{n=1}^{N} \sqrt{\alpha_n \beta_n \gamma}|^2 = N^2 \alpha\beta\gamma$; thus, the SNR grows quadratically with the number of RIS elements [24], [26]. The intuition behind this result is that the surface intercepts signal energy proportional to N (i.e., proportional to its area) and then focuses the reradiated signals to increase the received signal energy proportional to N (thanks to the constructive interference of the signals from the N elements). This result indicates that a physically large RIS is much more effective than a small one, which is fundamentally important since N^2 is multiplied with $\alpha\beta$, which is the product of two propagation losses that can be very small numbers.

A geometrical interpretation of the optimal RIS configuration is provided in Figure 3, where a plane wave is incident on a large, flat surface. If it is a homogeneous metal surface, as in Figure 3(a), the plane wave changes direction according to Snell's law but otherwise is unaffected (e.g., the two rays remain parallel). Each point on the surface reradiates the incident signal without causing any extra delays. In the illustrated scenario, the reflected signal does not reach the receiver. If the surface is replaced by an RIS, as in Figure 3(b), the optimized configuration focuses the reradiated signal at the receiver. The configuration in (30) adds extra delays in the center of the surface to make the propagation time to the receiver equal for all parallel rays that are reflected. As illustrated by the dashed line, the RIS is synthesizing how signals would have been reflected by a parabolic surface, where the length of each path via the surface is equal. This configuration will change the shape and main direction of the waveform (e.g., the two parallel incident rays have different directions when reradiated). The same effect could have been mechanically achieved by rotating and bending the flat metal surface, but doing so electronically using an

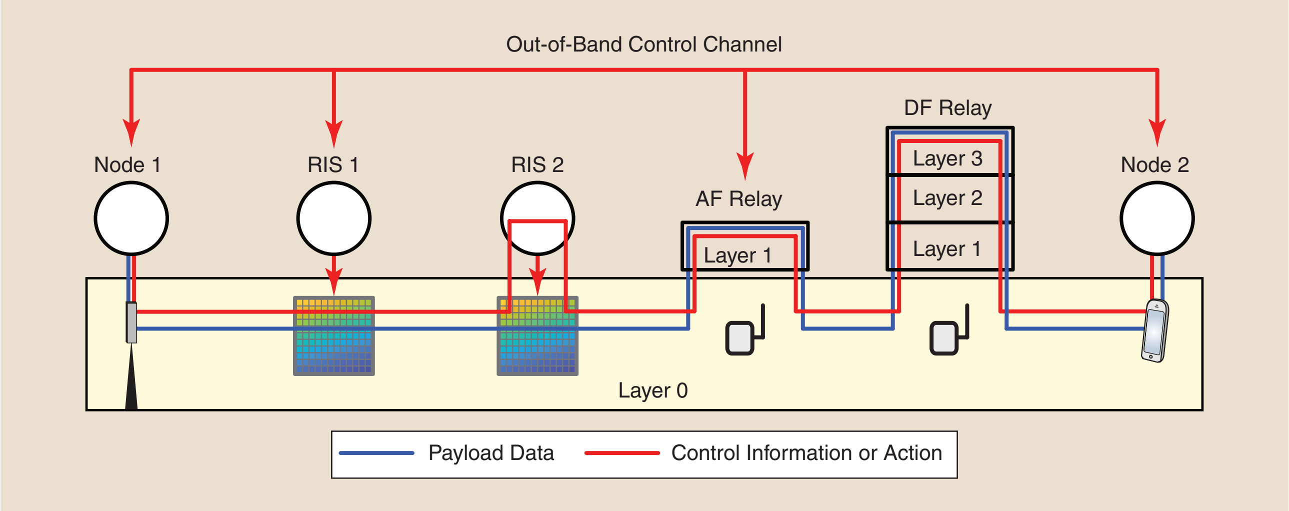

FIGURE 2. A layered perspective of the RIS and relay functionality. The wireless connection between node 1 and node 2 is supported by a cascade of RIS 1 with out-of-band control, RIS 2 with in-band control, amplify-and-forward (AF) relay, and decode-and-forward (DF) relay.

RIS adds great flexibility since different surface shapes can be synthesized at various times.

Narrowband capacity maximization with a partially uncontrollable channel

In practice, there are likely propagation paths between the transmitter and receiver not involving the RIS and thus outside its control. Recall from Figure 1(b) that these paths constitute the uncontrollable channel with impulse response $h_{d,\text{pb}}(t)$. In the narrowband case, the channel can be represented in the discrete-time complex pseudobaseband by an impulse response $\sqrt{\rho}\, e^{-\text{j}2\pi f_c \tau_d}$, where $\rho \in [0,1]$ is the propagation loss and $\tau_d \geq 0$ is the delay. We then obtain a memoryless AWGN channel with $h_{\boldsymbol{\theta}} = \sqrt{\rho}\, e^{-\text{j}2\pi f_c \tau_d} + \sum_{n=1}^{N} \sqrt{\alpha_n \beta_n \gamma}\, e^{-\text{j}2\pi f_c (\tau_{n,a} + \tau_{n,b} + \tau_{\theta_n})}$, for which the capacity in (27) becomes $B \log_2(1 + \text{SNR})$, with

$$\begin{aligned} \text{SNR} &= \frac{P}{BN_0} \left| \sqrt{\rho}\, e^{-\text{j}2\pi f_c \tau_d} + \sum_{n=1}^{N} \sqrt{\alpha_n \beta_n \gamma}\, e^{-\text{j}2\pi f_c (\tau_{n,a} + \tau_{n,b} + \tau_{\theta_n})} \right|^2 \\ &\leq \frac{P}{BN_0} \left| \sqrt{\rho}\, e^{-\text{j}2\pi f_c \tau_d} + \sum_{n=1}^{N} \sqrt{\alpha_n \beta_n \gamma}\, e^{-\text{j}2\pi f_c \tau_d} \right|^2 \\ &= \frac{P}{BN_0} \left| \sqrt{\rho} + \sum_{n=1}^{N} \sqrt{\alpha_n \beta_n \gamma} \right|^2. \end{aligned} \tag{31}$$

The upper bound is once again obtained by the Cauchy–Schwartz inequality, with the key difference that we cannot control the phase of the uncontrollable channel component. Hence, we need to select the delays of the RIS elements so that the N reradiated signals reach the receiver in phase with the signal received across the uncontrollable channel. Note that $e^{-\text{j}2\pi f_c \tau_d} = e^{-\text{j}2\pi f_c (\tau_{n,a} + \tau_{n,b} + \tau_{\theta_n})}$ holds if $\tau_{\theta_n} = \tau_d - \tau_{n,a} - \tau_{n,b}$ for $n = 1, \ldots, N$, but this results in a negative delay if the uncontrollable channel path is shorter than the paths via the RIS, which is usually the case. Therefore, to achieve a causal system implementation, we need to select the delays as $\tau_{\theta_n} = (\tau_d - \tau_{n,a} - \tau_{n,b}) + (k_n / f_c)$, where k_n is an integer such that $\tau_{\theta_n} \geq 0$; that is, $k_n \geq \lceil f_c (\tau_{n,a} + \tau_{n,b} - \tau_d) \rceil$, where $\lceil \cdot \rceil$ is the ceiling function. Then, the delay spread T_d is

$$\begin{aligned} T_\text{d} &= \max_{i=1,\ldots,N} \{\tau_{i,a} + \tau_{i,b} + \tau_{\theta_i}\} - \tau_d \\ &= \max_i \left\{ \frac{k_i}{f_c} \right\} \geq \max_i \left\{ \frac{1}{f_c} \lceil f_c (\tau_{i,a} + \tau_{i,b} - \tau_d) \rceil \right\}, \end{aligned} \tag{32}$$

which is minimized for the smallest integer that satisfies the preceding constraint [25].

The upper bound in (31) is achieved when the RIS configuration $\boldsymbol{\theta}$ can be selected from a continuous set. Suppose the RIS hardware restricts us to select τ_{θ_n} from a discrete set such that $2\pi f_c \tau_{\theta_n} \in \{\pi/2, 0, -\pi/2, -\pi\}$, as exemplified in Figure 1(b). The capacity maximization is now a combinatorial problem with 4^N possible configurations. Evaluating all options is computationally very complex, but a good heuristic is to rotate each term $e^{-\text{j}2\pi f_c (\tau_{n,a} + \tau_{n,b} + \tau_{\theta_n})}$ so that it is as close to $e^{-\text{j}2\pi f_c \tau_d}$ as possible. This leads to a partially coherent addition of the $N+1$ components of the channel $h_{\boldsymbol{\theta}}$. One can prove that the SNR loss is around only $8/\pi^2 = -0.9$ dB when having these four configurations [27], which implies that a small number of configurations per element is sufficient when implementing an RIS.

Figure 4 shows the capacities that can be achieved in a narrowband setup with $B = 1$ MHz and a varying number of RIS elements with $\gamma = 1$. The propagation losses via the RIS are $\alpha_n = -80$ dB and $\beta_n = -60$ dB, while $P/(BN_0) = 100$ dB. We consider two cases for the uncontrollable channel: –80 dB (strong) and –110 dB (weak). We notice that the RIS can increase the capacity by orders of magnitude when the uncontrollable channel is weak. The RIS-controlled path is 30 dB weaker than the uncontrollable path when $N = 1$, but since its contribution to the SNR grows as N^2, it surpasses the uncontrollable channel in strength when having $N = 32$ elements, and beyond that, the SNR grows as N^2. When the uncontrollable channel is strong, the capacity is already high, and the

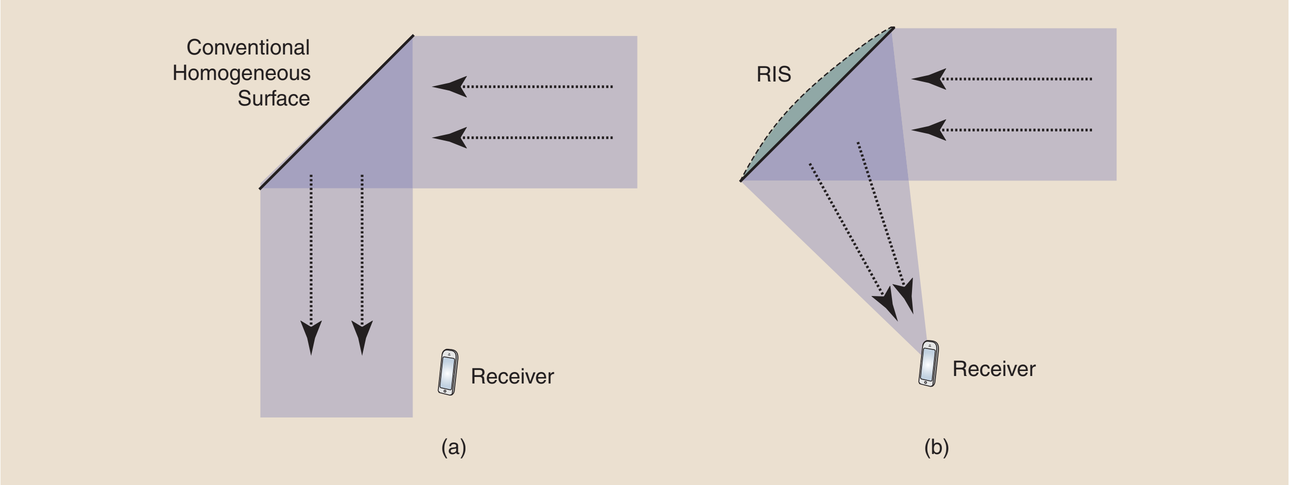

FIGURE 3. (a) A large, homogeneous, flat surface will reflect an incident plane wave in another direction, determined by Snell's law. Parallel incident rays remain parallel after reflection. (b) In contrast, an RIS of the same physical dimensions can be configured to synthesize the shape of a different object (here, a parabolic reflector), thereby controlling the direction and shape of the reflected waveform.

RIS has a limited effect on it because $N = 1{,}000$ elements are required before the path via the RIS becomes equally powerful. Figure 4 conveys results with the ideal RIS configuration and the case with only four phase shifts per element. The performance difference is small.

Reconfiguration under mobility

Most wireless channels are time variant due to user mobility. Yet, many properties of communication systems can be studied using LTI system theory by assuming (approximately) piecewise time-invariant channels, as done so far in this article. However, the study of Doppler effects due to mobility requires dropping the time invariance assumption and employing linear time-variant (LTV) system theory.

The nonlinear Doppler effect widens the signal bandwidth and can result in intersymbol interference, but we show that the RIS can mitigate some of these effects by varying its configuration to electronically synthesize movement, as illustrated in Figure 5. To show how to do that, we start by revisiting the passband input–output relationship for an arbitrary system in (1), which is given by the convolution equation for LTV filters [28]:

$$y_{\mathrm{pb}}(t) = \int_{-\infty}^{\infty} h_{\mathrm{pb}}(u,t)\, x_{\mathrm{pb}}(t-u)\, du, \tag{33}$$

where $h_{\mathrm{pb}}(\tau,t)$ is the real-valued time-varying impulse response, which can be regarded as a conventional LTI channel impulse response in τ that is slowly varying with the time t. While (33) is very similar to the convolution equation for LTI systems in (1), there is no direct correspondence to $Y_{\mathrm{pb}}(f)$ in (4). Instead, $y_{\mathrm{pb}}(t)$ is related to the frequency-domain representation of the passband input signal as

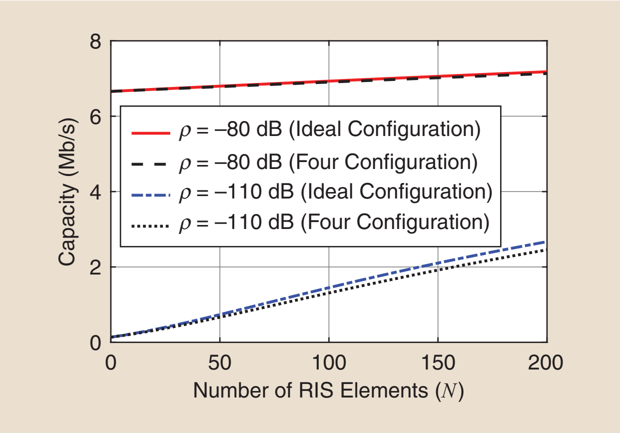

FIGURE 4. The capacity of a narrowband channel grows with the number of RIS elements. The benefit of controlling the channel using an RIS is particularly significant when the uncontrollable "direct" channel is weak.

$$y_{\mathrm{pb}}(t) = \int_{-\infty}^{\infty} H_{\mathrm{pb}}(f,t)\, X_{\mathrm{pb}}(f)\, e^{j2\pi f t}\, df, \tag{34}$$

where $H_{\mathrm{pb}}(f,t)$ is the time-variant transfer function, obtained as the Fourier transform of $h_{\mathrm{pb}}(\tau,t)$ with respect to τ. This function can be regarded as an LTI frequency response that varies slowly with t.

Consider the example system in Figure 1(b), and assume that the receiver is now a mobile user terminal. Then, the uncontrollable channel $h_{d,\mathrm{pb}}(\tau,t)$ and controllable channels from the RIS elements to the receiver $b_{n,\mathrm{pb}}(\tau,t), n = 1,\ldots,N$ are LTV filters. In contrast, the channels $a_{n,\mathrm{pb}}(\tau), n = 1,\ldots,N$ are still LTI filters since the transmitter and RIS are static. To show that an RIS can manage mobility, we need to drop the assumption that the configuration $\boldsymbol{\theta}$ is constant and consider each RIS element to also be an LTV filter with

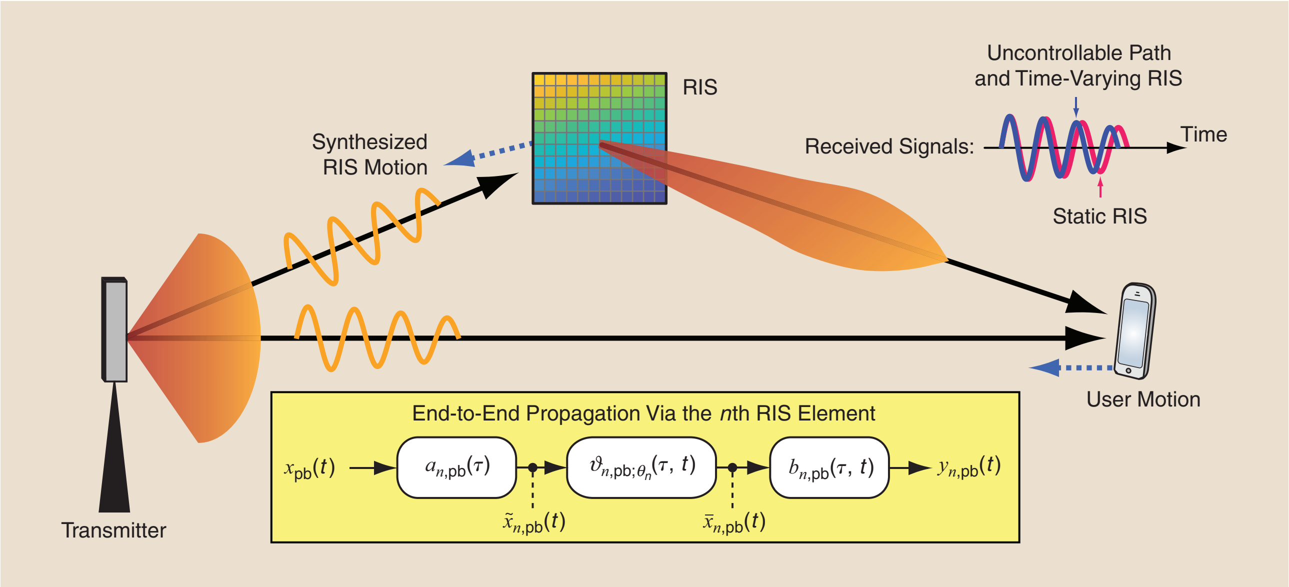

FIGURE 5. User motion creates a time-variant system, resulting in Doppler shifts. The shifts are generally different for the uncontrollable channel and the controllable channels via the RIS. However, the controllable channel can be configured to achieve zero Doppler spread by synthesizing RIS movement along a matching trajectory.

time-varying impulse response $\vartheta_{n,\text{pb};\theta_n}(\tau, t)$ and transfer function $\Theta_{n,\text{pb};\theta_n}(f, t) = \sqrt{\gamma_{\theta_n}(t)}\, e^{-j2\pi f \tau_{\theta_n}(t)}$, which is analogous to (20) except that γ_{θ_n} and τ_{θ_n} are now functions of the time t.

The resulting end-to-end propagation path across the nth RIS element is presented as a cascade of three systems in Figure 5. Computing the joint impulse response for this path is slightly more complicated than before due to the cascade of two LTV filters. To this end, we define the auxiliary signals $\tilde{x}_{n,\text{pb}}(t)$ and $\bar{x}_{n,\text{pb}}(t)$ as indicated in Figure 5, that is, as the outputs of the first and second filters, respectively. From the input–output relations in (33) and (34), it follows that the signal transmitted across the nth RIS element is

$$y_{n,\text{pb}}(t) = \int_{-\infty}^{\infty} b_{n,\text{pb}}(u, t)\bar{x}_{n,\text{pb}}(t-u)\, du, \tag{35}$$

$$= \int_{-\infty}^{\infty} b_{n,\text{pb}}(u, t)\Big(\int_{-\infty}^{\infty} \Theta_{n,\text{pb};\theta_n}(f, t-u)\tilde{X}_{n,\text{pb}}(f)\, e^{j2\pi f(t-u)} df\Big) du, \tag{36}$$

$$= \int_{-\infty}^{\infty} \underbrace{\Big(\int_{-\infty}^{\infty} b_{n,\text{pb}}(u, t)\Theta_{n,\text{pb};\theta_n}(f, t-u)\, e^{-j2\pi f u} du\Big) A_{n,\text{pb}}(f)}_{= H_{pb;\theta_n}(f,t)} X_{\text{pb}}(f)\, e^{j2\pi f t} df. \tag{37}$$

Observe that $\tilde{X}_{n,\text{pb}}(f)$ exists and is equal to $A_{n,\text{pb}}(f)X_{\text{pb}}(f)$ because the channel from the transmitter to the RIS element is still an LTI system. In (37), we can identify the joint time-varying transfer function $H_{\text{pb};\theta_n}(f, t)$ of the nth RIS propagation path. Its corresponding time-variant impulse response $h_{\text{pb};\theta_n}(\tau, t)$ is obtained from the inverse Fourier transform with respect to f. Then, due to the linearity, the time-varying impulse response of the end-to-end system in (33) is $h_{\text{pb};\boldsymbol{\theta}}(\tau, t) = h_{d,\text{pb}}(\tau, t) + \sum_{n=1}^{N} h_{\text{pb};\theta_n}(\tau, t)$.

The obtained input–output relation holds for all LTV systems. Let us now assume a narrowband channel with $A_{n,\text{pb}}(f) = \sqrt{\alpha_n}\, e^{-j2\pi f \tau_{n,a}}$ and $b_{n,\text{pb}}(\tau, t) = \sqrt{\beta_n(t)}\, \delta(\tau - \tau_{n,b}(t))$. Then, the channel across the nth RIS element has the transfer function

$$H_{\text{pb};\theta_n}(f, t) = \sqrt{\alpha_n \gamma_{\theta_n}(t)\beta_n(t)}\, e^{-j2\pi f(\tau_{n,a} + \tau_{\theta_n}(t) + \tau_{n,b}(t))}, \tag{38}$$

where we utilize the fact that the RIS element's transfer function can be arbitrarily translated in time. Using this result, the channel output is straightforwardly obtained as

$$\begin{aligned} y(t) = {} & \sqrt{\rho(t)}\, e^{-j2\pi f_c \tau_d(t)} x(t - \tau_d(t)) \\ & + \sum_{n=1}^{N} \sqrt{\alpha_n \gamma_{\theta_n}(t)\beta_n(t)}\, e^{-j2\pi f_c(\tau_{n,a} + \tau_{\theta_n}(t) + \tau_{n,b}(t))} \\ & \cdot x(t - \tau_{n,a} - \tau_{\theta_n}(t) - \tau_{n,b}(t)). \end{aligned} \tag{39}$$

This system model enables us to study the optimal RIS configuration, taking mobility effects into account. First, consider the case with only a controllable channel; that is, $\rho(t) = 0$ for all t. Recall from (29) that the capacity-maximizing configuration in this scenario is $\tau_{\theta_n}(t) = \varrho_n(t) - \tau_{n,a} - \tau_{n,b}(t)$, where $\varrho_n(t)$ is chosen such that the signals from the N RIS elements reach the receiver with aligned phases. The solution that achieves this with minimum delay was determined in (30) as $\varrho_n(t) = \max_{i=1,\dots,N}\{\tau_{i,a} + \tau_{i,b}(t)\}$ for all n. When this solution is applied under mobility, the pointwise maximum operation will occasionally lead to discontinuities with sudden phase jumps. Avoiding this requires restricting the phase shifts induced by $\varrho_n(t)$ to integer multiples of 2π; that is, $\varrho_n(t) = k_n(t)/f_c$, with $k_n(t)$ being a piecewise constant function taking integer values. Moreover, causality requires all $\tau_{\theta_n}(t)$ to be nonnegative. Thus, the delay is minimized by $k_n(t) = \max_{i=1,\dots,N}\lceil f_c(\tau_{i,a} + \tau_{i,b}(t))\rceil$ for all n. This increases the propagation delay by at most one period of the carrier signal compared to the delay-minimizing configuration, avoids undesired spectral effects, and does not introduce any extra delay spread. Moreover, we have $x(t - \tau_d(t)) \approx x(t - \tau_{n,a} - \tau_{\theta_n}(t) - \tau_{n,b}(t))$ as long as the symbol time is much larger than the delay spread.

Another phenomenon that occurs only under mobility is the Doppler shift. For each propagation path, the Doppler shift is defined as the difference between the observed and emitted frequency:

$$\begin{aligned} \mathcal{D}_n &= -\frac{d}{dt}[f_c(\tau_{n,a} + \tau_{\theta_n}(t) + \tau_{n,b}(t))] \\ &= -f_c \frac{d(\tau_{\theta_n}(t) + \tau_{n,b}(t))}{dt}. \end{aligned} \tag{40}$$

Interestingly, the Doppler shift can be fully compensated for by the RIS by tuning the delays such that the RIS counteracts the rate of change of $\tau_{n,b}(t)$; that is, each RIS element needs to implement $\tau_{\theta_n}(t)$ such that $d\tau_{\theta_n}(t)/dt = -d\tau_{n,b}(t)/dt$. This technique is known as *Doppler cloaking* and leads to the Doppler effect being unobservable in the received signal. It has been investigated in different contexts to reduce electromagnetic noise caused by objects moving toward radar and sonar systems and even to build invisibility cloaks for moving objects [29]. Possible applications in communication systems could be to deploy legacy systems in high-mobility scenarios they where not designed for and connect Internet-of-Things devices with very simple transceiver chains to fast-moving satellites in space.

For the SNR-optimal configuration with minimum delay derived earlier, we obtain the Doppler shift

$$\mathcal{D}_n = -f_c\left[\frac{d}{dt}\left(\frac{k_n(t)}{f_c} - \tau_{n,a} - \tau_{n,b}(t)\right) + \frac{d\tau_{n,b}(t)}{dt}\right] = -\frac{dk_n(t)}{dt}. \tag{41}$$

Because changes in $k_n(t)$ do not lead to phase discontinuities, there is no effect on the Doppler shift, and $dk_n(t)/dt$ can be assumed to be zero from a practical perspective. Hence, this configuration maximizes the SNR with minimum delay and removes Doppler shifts [25]. Next, consider the case with an additional uncontrollable propagation path [i.e., $\rho(t) \neq 0$], again under the assumption that it is shorter than the RIS path. Following the previous discussion, the SNR-optimal configuration with minimum delay is $\tau_{\theta_n}(t) = (\tau_d(t) - \tau_{n,a} - \tau_{n,b}(t)) + k_{n,\min}(t)/f_c$, where $k_{n,\min}(t)$ is the minimum integer that satisfies the causality constraint; that is, $k_{n,\min}(t) =$

$[f_c(\tau_{n,a}+\tau_{n,b}-\tau_d)]$. Using this configuration and employing (40), the Doppler shift of the propagation path across the nth RIS element is $\mathcal{D}_n = -f_c(d\tau_d(t)/dt)$, where we omit $(dk_{n,\min}(t)/dt)$ for the same reason as before. This is the same as the Doppler shift of the uncontrollable channel, and hence the Doppler spread is zero.

It is impossible to simultaneously maximize the SNR and compensate for the Doppler shifts introduced by the RIS (as is the case without an uncontrollable path). However, even if it were possible, it would be undesired, as it results in a Doppler spread of $f_c(d\tau_d(t)/dt)$. Since the mitigation of Doppler spreads is usually much more difficult than treating Doppler shifts at the receiver, having the RIS not introducing additional Doppler spread in the system could be considered the optimal solution in terms of Doppler effects. In conclusion, we have observed that the SNR-optimal configuration with minimum delay obtained using the developed LTI system model is still valid and optimal when mobility is involved. While some care has to be taken not to introduce additional frequency components into the spectrum due to phase discontinuities, an SNR-maximizing configuration also minimizes the delay spread and does not introduce additional Doppler spread into the system.

RIS design for wideband capacity maximization

RIS optimization becomes more challenging in the wideband case, where there are K parallel subcarriers, each represented by the system model in (16). The subcarriers are separate AWGN channels but share the power P since they are simultaneously transmitted. Suppose the power $P_\nu = \mathbb{E}\{|\bar{x}[\nu]|^2\}$ is assigned to subcarrier ν. Any power allocation $P_0,\dots,P_{K-1}$ satisfying $P = \Sigma_{\nu=0}^{K-1} P_\nu / K$ is feasible.

When studying this setup, we make use of the frequency response in (23) for the controllable channel via the RIS, but we also add an uncontrollable channel. We let $\boldsymbol{h}_d = [h_d[0],\dots,h_d[M-1]]^{\mathrm{T}}$ denote the discrete-time impulse response of the uncontrollable channel, which can be computed similarly to (21): $h_d[k] = \Sigma_{l=1}^{L_d} \sqrt{\rho^l}\, e^{-j2\pi f_c \tau_d^l} \operatorname{sinc}(k + B(\eta - \tau_d^l))$, where L_d is the number of paths, $\rho^l \in [0,1]$ is propagation loss of the lth path, and $\tau_d^l \geq 0$ is its delay.

For a given RIS configuration $\boldsymbol{\theta}$ and power allocation, the so-called achievable rate is

$$R = \frac{B}{K+M-1} \sum_{\nu=0}^{K-1} \log_2\left(1 + \frac{P_\nu \left| \boldsymbol{f}_\nu^{\mathrm{H}} \boldsymbol{h}_d + \boldsymbol{f}_\nu^{\mathrm{H}} \boldsymbol{V}^{\mathrm{T}} \boldsymbol{\omega}_{\boldsymbol{\theta}} \right|^2}{BN_0}\right) \text{ bit/s}, \tag{42}$$

where $\boldsymbol{f}_\nu^{\mathrm{H}}$ is the νth row of the DFT matrix $\boldsymbol{F}$. This rate expression is a summation across the K subcarriers, which is then divided by $K+M-1$ (instead of K) to compensate for the cyclic prefix loss. The capacity is obtained by maximizing this expression with respect to both the power allocation and RIS configuration. The former is a classical problem with a solution called *water-filling power allocation* [30]:

$$P_\nu = \max\left(\mu - \frac{BN_0}{\left|\boldsymbol{f}_\nu^{\mathrm{H}} \boldsymbol{h}_d + \boldsymbol{f}_\nu^{\mathrm{H}} \boldsymbol{V}^T \boldsymbol{\omega}_{\boldsymbol{\theta}}\right|^2}, 0\right), \tag{43}$$

where the parameter $\mu \geq 0$ is selected to make $\Sigma_{\nu=0}^{K-1} P_\nu / K = P$.

The maximization of (42) with respect to the RIS configuration $\boldsymbol{\theta}$ entails selecting the most preferred vector $\boldsymbol{\omega}_{\boldsymbol{\theta}}$ among those that the hardware can generate. Note that the same vector affects all subcarriers because the transmissions are simultaneous. In the narrowband case, we could optimize the RIS in closed form since there was only one channel (one subcarrier), but now we need to find a nontrivial tradeoff between all K subcarriers. So far, this problem seems mathematically intractable to solve to global optimality; thus, the literature contains heuristic solutions based on successive convex approximation, semidefinite relaxation, and strongest tap maximization (STM) in the time domain [30]–[32]. In this article, we focus on the STM solution from [31] and [32] and compare it against an upper bound.

The intuition behind STM is that the received signal power is spread out across the K subcarriers but rather concentrated in the time domain since $M \ll K$ [31]. Hence, selecting a configuration $\boldsymbol{\theta}$ that is good for one strong channel tap is better than an arrangement that is good for one strong subcarrier. This is particularly true when there is an LOS propagation path that is much stronger than all the other paths. When adding the uncontrollable channel to (22), the ℓth tap of the impulse response becomes $h_d[\ell] + \boldsymbol{v}_\ell^{\mathrm{T}} \boldsymbol{\omega}_{\boldsymbol{\theta}}$. We begin by finding the value of $\boldsymbol{\omega}_{\boldsymbol{\theta}}$ that maximizes the magnitude of each tap:

$$\boldsymbol{\omega}_\ell = \underset{\boldsymbol{\omega}_{\boldsymbol{\theta}}}{\operatorname{argmax}} \left| h_d[\ell] + \boldsymbol{v}_\ell^{\mathrm{T}} \boldsymbol{\omega}_{\boldsymbol{\theta}} \right|, \quad \ell = 0,\dots,M-1. \tag{44}$$

In STM, we then select the solution from candidates $\boldsymbol{\omega}_0,\dots,\boldsymbol{\omega}_{M-1}$ that results in the largest magnitude:

$$\boldsymbol{\omega}_{\mathrm{STM}} = \boldsymbol{\omega}_{\ell^{\mathrm{opt}}} \quad \text{where } \ell^{\mathrm{opt}} = \underset{\ell \in \{0,\dots,M-1\}}{\operatorname{argmax}} \left| h_d[\ell] + \boldsymbol{v}_\ell^{\mathrm{T}} \boldsymbol{\omega}_\ell \right|. \tag{45}$$

Each of the subproblems in (44) can be analogously solved with the narrowband SNR maximization in (31). The solution is $\boldsymbol{\omega}_\ell = [e^{\mathrm{j}(\arg(h_d[\ell]) - \arg([\boldsymbol{v}_\ell]_1))}, \dots, e^{\mathrm{j}(\arg(h_d[\ell]) - \arg([\boldsymbol{v}_\ell]_N))}]^{\mathrm{T}}$, where $[\boldsymbol{v}_\ell]_n$ denotes the nth entry of $\boldsymbol{v}_\ell$ and $\arg(\cdot)$ gives the argument (phase) of a complex number. Note that this solution rotates the phase of each term in the inner product $\boldsymbol{v}_\ell^{\mathrm{T}} \boldsymbol{\omega}_\ell$ so that it matches with the phase of $h_d[\ell]$.

To evaluate the quality of the heuristic STM solution, we can compare the rate that it achieves with an upper bound. Suppose we could select a different value of $\boldsymbol{\omega}_{\boldsymbol{\theta}}$ on each subcarrier. We could then jointly maximize the SNRs of all subcarriers. For the νth subcarrier, its SNR is maximized by selecting $\boldsymbol{\omega}_{\boldsymbol{\theta}} = [e^{\mathrm{j}(\arg(\boldsymbol{f}_\nu^{\mathrm{H}} \boldsymbol{h}_d) - \arg([\boldsymbol{f}_\nu^{\mathrm{H}} \boldsymbol{V}^{\mathrm{T}}]_1))}, \dots, e^{\mathrm{j}(\arg(\boldsymbol{f}_\nu^{\mathrm{H}} \boldsymbol{h}_d) - \arg([\boldsymbol{f}_\nu^{\mathrm{H}} \boldsymbol{V}^{\mathrm{T}}]_N))}]^{\mathrm{T}}$. The resulting upper bound is

$$R \leq \frac{B}{K+M-1} \sum_{\nu=0}^{K-1} \log_2\left(1 + \frac{P_\nu}{BN_0}\left(\left|\boldsymbol{f}_\nu^{\mathrm{H}} \boldsymbol{h}_d\right| + \left\|\boldsymbol{f}_\nu^{\mathrm{H}} \boldsymbol{V}^{\mathrm{T}}\right\|_1\right)^2\right), \tag{46}$$

where $\|\cdot\|_1$ denotes the L_1 norm. This upper bound is exactly achievable only in the unlikely event that the same RIS configuration happens to maximize the SNRs of all subcarriers.

Figure 6 gives simulation results for the achievable rates across a wideband channel, inspired by the setup in Figure 1(b). The RIS and receiver are located in a large room and thus have an LOS channel between them. The transmitter is an access point located 400 m away and has a non-LOS (NLOS) channel to the receiver. We consider cases where the transmitter-to-RIS channel is either LOS or NLOS. The carrier frequency is 3 GHz, and the RIS is 0.5×0.5 m, which corresponds to $N = 400$ elements that each have dimension $\lambda/4 \times \lambda/4$. The channels are modeled similarly to the 3rd Generation Partnership Project (3GPP) channel model in [33], and the rate is averaged across random realizations of the multipath components. The rate in (42) appears in Figure 6 as a function of the bandwidth B. The optimal water-filling power allocation from (43) is utilized, and the transmit power P grows proportionally to the bandwidth. The subcarrier spacing is 150 kHz; thus, the number of subcarriers increases with B as well as the number of channel taps.

Figure 6(a) considers the case with an LOS path from the transmitter to the RIS. The dashed curve represents the rate when using the heuristic STM configuration of the RIS. It provides 96–98% of the upper bound from (46). The gap grows with B, due to the increased frequency selectivity, but since the LOS paths to/from the RIS are stronger than the scattered paths, it is possible to find a single-RIS configuration that works well across the entire band. The refined RIS configuration algorithms described in [30]–[32] can reduce the gap but improve the rate by only a few percent. It is interesting to compare the rate with what could be achieved without an RIS. In this case, we can replace the RIS with either an absorbing material, thereby removing all the paths via the RIS, or a passive metal sheet causing zero phase shifts. The corresponding curves in Figure 6(a) nearly overlap, but there are ideal situations where a perfectly rotated metal sheet is almost as efficient as an RIS [18]. The RIS can increase the rate by 2.7–2.9 times, which makes a huge difference when there are several megahertz of bandwidth.

Figure 6(b) considers the case with an NLOS path from the transmitter to the RIS, which has two effects: the path via the RIS is weaker, and there is no dominant path. The former effect results in a much smaller gap between the upper bound and "no RIS" cases, while the latter results in an inability to find a single-RIS configuration that fits the entire band. In this case, the RIS can improve the rate by 4% in the narrowband case of $B = 400$ kHz, but the gain vanishes as B increases. One can find a slightly better RIS configuration using the algorithms in [30]–[32], but the bottom line is that an RIS must be carefully deployed to be truly effective. It should be deployed, as in Figure 6(a), at a location with an LOS to the access point, and it can then be configured to greatly improve the rate to users that are within the LOS of it.

Protocol for channel estimation and reconfiguration

Capacity maximization has been described above assuming that the channels are perfectly known, but a preceding channel estimation phase is required in practice. Since the RIS is passive, the estimation must be carried out at the receiver. If we focus on the OFDM case and neglect the uncontrollable channel, the frequency response in (23) is $\bar{\boldsymbol{h}}_{\boldsymbol{\theta}} = \boldsymbol{F}\boldsymbol{V}^{\mathrm{T}}\boldsymbol{\omega}_{\boldsymbol{\theta}}$, where the matrix $\boldsymbol{V}$ represents the cascade of the channel from the transmitter to the RIS and the channel from the RIS to the receiver. It is sufficient to estimate $\boldsymbol{V}$ to compute $\bar{\boldsymbol{h}}_{\boldsymbol{\theta}}$ for any $\boldsymbol{\omega}_{\boldsymbol{\theta}}$, which is fortunate since it is hard to resolve the individual channels.

Suppose a known pilot signal x is transmitted on each of the M subcarriers, where M equals the number of (unknown)

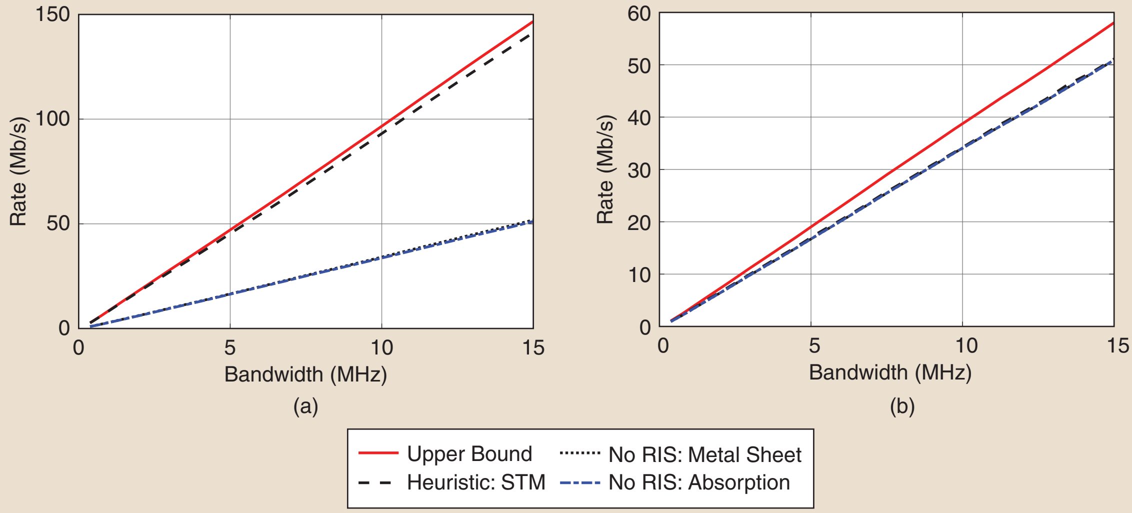

(a)

(b)

FIGURE 6. The rate that can be achieved across a wideband channel grows proportionally to the bandwidth. LOS channels to and from the RIS can greatly improve the slope and achieve a rate close to the upper bound in (46). This performance gain collapses if there is a non-LOS (NLOS) path to the RIS. (a) An LOS channel from the transmitter to the RIS. (b) An NLOS channel from the transmitter to the RIS.

terms in the time-domain channel $\boldsymbol{h}_{\boldsymbol{\theta}}$. Let the RIS configuration be $\boldsymbol{\theta}_t$, where t is the index of the OFDM block. The received signal $\bar{z}[t] \in \mathbb{C}^M$ across the M pilot-bearing subcarriers at OFDM block t is

$$\bar{z}[t] = \boldsymbol{F}_M \boldsymbol{V}^{\mathrm{T}} \boldsymbol{\omega}_{\boldsymbol{\theta}_t} x + \bar{\boldsymbol{w}}[t], \tag{47}$$

where $\boldsymbol{F}_M$ contains the M rows of $\boldsymbol{F}$ corresponding to the selected subcarriers and $\bar{\boldsymbol{w}}[t] \in \mathbb{C}^M$ contains the corresponding noise. There are MN unknown parameters in $\boldsymbol{V}$, but we obtain only M observations from $\bar{z}[t]$. Using more than M subcarriers for pilot transmission will not resolve this issue since the impact of the RIS configuration $\boldsymbol{\omega}_{\boldsymbol{\theta}_t}$ cannot be removed from (47); a vector is noninvertible. The way to get MN linearly independent observations, where N is the number of RIS elements, is to consider a sequence of N OFDM blocks with different configurations: $\boldsymbol{\theta}_1, \ldots, \boldsymbol{\theta}_N$. The joint received signal is

$$\underbrace{[\bar{z}[1], \ldots, \bar{z}[N]]}_{=\bar{\boldsymbol{Z}}} = \boldsymbol{F}_M \boldsymbol{V}^{\mathrm{T}} \underbrace{[\boldsymbol{\omega}_{\boldsymbol{\theta}_1}, \ldots, \boldsymbol{\omega}_{\boldsymbol{\theta}_N}]}_{=\boldsymbol{\Omega}} x + \underbrace{[\bar{\boldsymbol{w}}[1], \ldots, \bar{\boldsymbol{w}}[N]]}_{=\bar{\boldsymbol{W}}}. \tag{48}$$

If the RIS configurations are selected so that $\boldsymbol{\Omega}$ is invertible (e.g., a DFT matrix), we can rewrite (48) as

$$\underbrace{\frac{1}{x} \boldsymbol{F}_M^{-1} \bar{\boldsymbol{Z}} \boldsymbol{\Omega}^{-1}}_{\text{Known signal}} = \boldsymbol{V}^{\mathrm{T}} + \underbrace{\frac{1}{x} \boldsymbol{F}_M^{-1} \bar{\boldsymbol{W}} \boldsymbol{\Omega}^{-1}}_{\text{Noise}}. \tag{49}$$

This is a linear model from which a variety of classical channel estimation techniques can be applied. In fact, (49) is already the least-square estimate of $\boldsymbol{V}^{\mathrm{T}}$. If there is prior information, such as a fading distribution and spatial–temporal sparsity, this can be used to devise better estimators that also require shorter pilots [5], [19], [34]. Since switching between configurations is a nonlinear operation and thus can modulate the reflected signals into other bands, it should be done in a silent guard interval between OFDM blocks. After the receiver has estimated the channel, it can compute a suitable configuration $\boldsymbol{\omega}_{\boldsymbol{\theta}}$ (as described earlier) that can be utilized as long as the channel remains static. The control channel described in Figure 2 can be used to inform the RIS of the desired configuration. Because only M out of K subcarriers are used for pilots, the remaining ones can carry data. To handle mobility, one can develop protocols for progressive RIS reconfiguration, where data are continuously transmitted and pilots are sent at regular intervals to re-estimate the channel and reconfigure the RIS [31], [32].

RIS-aided localization and sensing

We will now consider localization and sensing. The objective of localization is to estimate and track the position of an actively communicating user device, while the objective of sensing is to estimate and track the location of passive objects and users. All radio localization and sensing systems operate under common principles: there are location references, dynamic user states, and measurements, which are connected to the user state via a statistical model. The development of a radio localization system has three main components: design, channel estimation, and localization/sensing. Design includes the placement and configuration of reference points and the arrangement of pilot signals to maximize localization accuracy. It can be offline but also online to adapt to user locations and requirements. An important tool in the design phase is Fisher information theory [35].

Channel parameter estimation is usually performed prior to localization and sensing and involves the approximation of geometric parameters (e.g., delays, angles, and frequency shifts) from received signals. Note that both localization and communication rely on channel knowledge. However, localization explicitly determines the geometric parameters, while the unstructured channel (49) is sufficient for communication. Location estimation, sensing, and tracking are performed after channel estimation, with the aim to invert the geometric relation between a user's location and the channel parameter estimates to recover the user's position as well as the state of passive objects. Tracking algorithms (e.g., the extended Kalman filter) are used to recursively update these locations through time. Localization and sensing most often involve the determination of nuisance parameters (e.g., synchronization and other biases as well as data associations among measurements and objects), leading to high-dimensional and nonlinear optimization problems. While a detailed treatment of localization and tracking techniques is beyond the scope of this article, we provide a brief overview of localization and sensing without an RIS in 4G and 5G to contrast with the potential benefits that an RIS brings.

Localization and sensing in 4G and 5G

Every new generation of mobile communications introduces new features for higher-rate transmission that also enable more accurate localization [36], as visualized in Figure 7. In 4G systems, localization is based on the transmissions of pilot signals sent by multiple synchronized BSs across orthogonal subcarriers. The pilot design is such that it covers the entire signal bandwidth and avoids inter-BS interference. A user estimates the time-of-arrival (TOA) with respect to each BS, which depends on the distance to the BS and the user's clock bias. Estimating TOAs from at least four BSs in LOS enables the user to compute three time-difference-of-arrival (TDOA) measurements and solve for its 3D location. The estimation accuracy depends on the SNR as well as the bandwidth spanned by the pilot signals, which determines the sampling rate and thereby the resolvability of the multipath components in time. In fact, multipath limits the accuracy to tens of meters in 4G [36]. In systems with a large bandwidth, individual multipath components can be resolved and related to physical objects [e.g., a scatter point (SP)] in the environment [37].

In 5G systems operating in millimeter-wave (mm-wave) bands, a BS and possibly a user are equipped with multiple antennas [38]. The channel is then parameterized by delays (as in 4G) and angles: angles-of-arrival (AOA) at the receiver and angles-of-departure (AOD) at the transmitter, both in azimuth and elevation. This means that the user can be localized from the AOD of two BSs (by the intersection of two lines), significantly reducing infrastructure needs. The channel parameter measurements can be related to objects in the environment with unknown 3D locations through simultaneous localization and mapping. In contrast to 4G, which must collect measurements through time [37], the additional angle measurements in 5G enable sensing the environment from a single snapshot of observations [3], [39]. Despite the high interest in mm-wave bands in 5G, it is important to note that lower-frequency bands remain relevant due to their large coverage and support for spatial multiplexing of many users. For dense multipath environments, it is challenging to resolve individual propagation paths, limiting the use of lower bands to favorable propagation environments (e.g., outdoors) and requiring data-driven fingerprinting techniques.

Localization and sensing with an RIS

The inclusion of an RIS provides several opportunities for localization [8], [40], including new synchronized location references and configurations for optimizing localization performance. Each RIS also leads to several novel geometric measurements, which, in turn, improve localization accuracy and coverage. The 5G scenario in Figure 7 is easily generalized to one with an RIS [41], making the problem highly overdetermined and in a sense easier. Thus, we focus on the more refined and challenging case with one single-antenna transmitting BS, one single-antenna receiving user, and one RIS with N elements. While communication uses approximately sinc-shaped pulses that are bandwidth-efficient, localization employs roughly square-shaped pulses because these are easier to distinguish in time.

Suppose the uncontrollable channel from the transmitter (i.e., the BS) to the receiver (i.e., the user) consists of L_d propagation paths, where $\rho^l \in [0,1]$ is the propagation loss and $\tau_d^l \geq 0$ is the delay of the lth path. The first one is the LOS path. Furthermore, the RIS is in the far field, and there is only an LOS path to/from the RIS (i.e., $L_a = L_b = 1$), where τ_{RIS} denotes the propagation delay via the first element. Under these circumstances, if $\bar{\boldsymbol{x}} \in \mathbb{C}^K$ is the transmitted pilot signal across the K subcarriers, the received signal $\bar{z}[t]$ in the OFDM block with index t is

$$\bar{z}[t] = \underbrace{\sum_{l=1}^{L_d} g^l \boldsymbol{d}(\tau_d^l) \odot \bar{\boldsymbol{x}}}_{\text{Uncontrollable channel}} + \underbrace{\boldsymbol{v}^{\mathrm{T}} \boldsymbol{\omega}_{\boldsymbol{\theta}} (\boldsymbol{d}(\tau_{\mathrm{RIS}}) \odot \bar{\boldsymbol{x}})}_{\text{Controllable channel}} + \bar{\boldsymbol{w}}[t], \quad (50)$$

where $\odot$ is the Hadamard product and $g^l = \sqrt{\rho^l}\, e^{-j2\pi f_c \tau_d^l}$ is the complex channel gain of path l. Here, $\boldsymbol{d}(\tau) \in \mathbb{C}^K$, with $[\boldsymbol{d}(\tau)]_\nu = e^{-j2\pi\tau\Delta_f \nu}$, where $\Delta_f = B/K$ is the subcarrier spacing. The vectors $\boldsymbol{v} \in \mathbb{C}^N$ and $\boldsymbol{\omega}_{\boldsymbol{\theta}} \in \mathbb{C}^N$ are defined in (22), except that the subscript k as been dropped.

Due to the far-field LOS assumption, we have $\alpha_n = \alpha$ and $\beta_n = \beta$ for all n, and we can make use of the steering vector of the RIS. Recall that we term it $\boldsymbol{a}(\boldsymbol{\phi}) \in \mathbb{C}^N$, where $\boldsymbol{\phi} = [\phi^{\mathrm{az}}, \phi^{\mathrm{el}}]^{\mathrm{T}} \in \mathbb{R}^2$ contains the azimuth and elevation angle. The steering vector gives the phase shifts between the RIS elements for a plane wave impinging from $\boldsymbol{\phi}$. If we further assume that the fraction of reradiated power from all RIS elements is identical, i.e., $\gamma_{\theta_n} = \gamma$ in $\boldsymbol{\omega}_{\boldsymbol{\theta}}$, we can write $\boldsymbol{v}^{\mathrm{T}} \boldsymbol{\omega}_{\boldsymbol{\theta}}$ in (50) as

$$\boldsymbol{v}^T \boldsymbol{\omega}_{\boldsymbol{\theta}} = g_{\mathrm{RIS}} \Big(\underbrace{\boldsymbol{a}(\boldsymbol{\phi}_a) \odot \boldsymbol{a}(\boldsymbol{\phi}_b)}_{=\boldsymbol{b}(\boldsymbol{\phi}_b)} \Big)^{\mathrm{T}} \bar{\boldsymbol{\omega}}_{\boldsymbol{\theta}}, \quad (51)$$

where $g_{\mathrm{RIS}} = \sqrt{\alpha\beta\gamma}\, e^{j\psi_{\mathrm{RIS}}}$ with ψ_{RIS} is a global phase shift and $\boldsymbol{\phi}_a = [\phi_{\mathrm{a}}^{\mathrm{az}}, \phi_{\mathrm{a}}^{\mathrm{el}}]^{\mathrm{T}} \in \mathbb{R}^2$ and $\boldsymbol{\phi}_b = [\phi_{\mathrm{b}}^{\mathrm{az}}, \phi_{\mathrm{b}}^{\mathrm{el}}]^{\mathrm{T}} \in \mathbb{R}^2$ are the

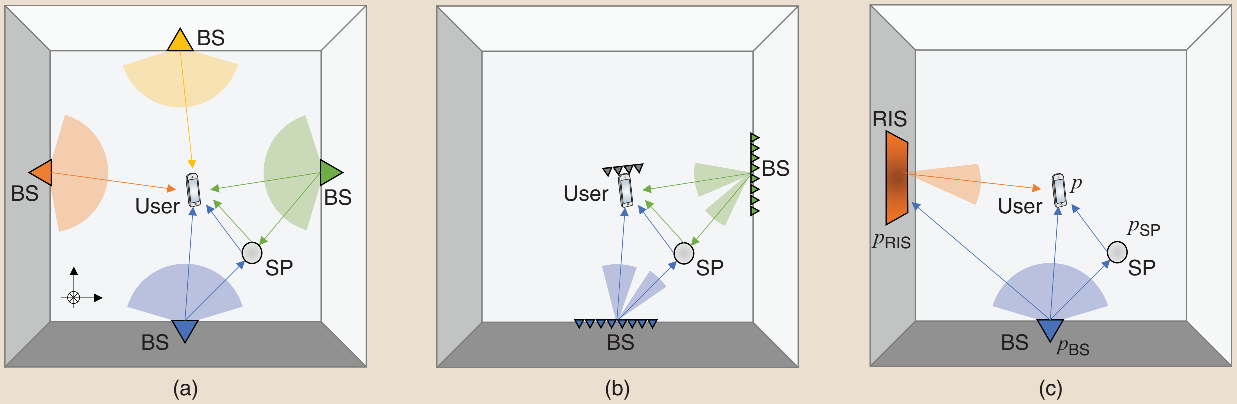

FIGURE 7. Localization and sensing across generations of mobile communication technology. (a) 4G relies on multiple BSs to obtain time-difference-of-arrival measurements. Uncontrollable multipath components, represented here by a scatter point (SP), become a disturbance. (b) In 5G, the inclusion of angle-of-arrival and angle-of-departure measurements reduces infrastructure needs and enables the sensing of the environment. (c) Beyond 5G, a scenario with a single BS and an RIS is shown. This infrastructure is sufficient to localize a user and provide partial map information if we exploit the fact that the RIS path is controllable.

(azimuth and elevation) AOA and AOD at the RIS, respectively. The vector $\bar{\boldsymbol{\omega}}_{\boldsymbol{\theta}} \in \mathbb{C}^N$ is obtained from $\boldsymbol{\omega}_{\boldsymbol{\theta}}$ by setting $\gamma_n = 1$ for all n and thus has entries on the unit circle. If the geographical locations $\boldsymbol{p}_{\text{BS}} \in \mathbb{R}^3$ and $\boldsymbol{p}_{\text{RIS}} \in \mathbb{R}^3$ of the BS and RIS, respectively, are known, so is the AOA $\boldsymbol{\phi}_a$, and we use the notation $\boldsymbol{b}(\boldsymbol{\phi}_b) = \boldsymbol{a}(\boldsymbol{\phi}_a) \odot \boldsymbol{a}(\boldsymbol{\phi}_b)$ in (51) to focus on the unknown angle $\boldsymbol{\phi}_b$.

In the preceding system model, there are $3L_d + 5$ real unknown parameters: $L_d + 1$ complex channel gains $\{g_{\text{RIS}}, g^l : l = 1,\ldots,L_d\}$, $L_d + 1$ delays $\{\tau_{\text{RIS}}, \tau_d^l : l = 1,\ldots,L_d\}$, and a 2D AOD vector $\boldsymbol{\phi}_b$. Let $\boldsymbol{p} \in \mathbb{R}^3$ denote the unknown user location and $\boldsymbol{p}_{\text{SP},l} \in \mathbb{R}^3$ represent the location of the lth SP, for $l = 2,\ldots,L_d$. These location parameters are related to the system model parameters as follows:

$$\tau_d^1 = \frac{\| \boldsymbol{p}_{\text{BS}} - \boldsymbol{p} \|}{c} + \Delta_{\text{clk}}, \tag{52}$$

$$\tau_d^l = \frac{\| \boldsymbol{p}_{\text{BS}} - \boldsymbol{p}_{\text{SP},l} \|}{c} + \frac{\| \boldsymbol{p}_{\text{SP},l} - \boldsymbol{p} \|}{c} + \Delta_{\text{clk}}, \quad l > 1, \tag{53}$$

$$\tau_{\text{RIS}} = \frac{\| \boldsymbol{p}_{\text{BS}} - \boldsymbol{p}_{\text{RIS}} \|}{c} + \frac{\| \boldsymbol{p} - \boldsymbol{p}_{\text{RIS}} \|}{c} + \Delta_{\text{clk}}, \tag{54}$$

$$\boldsymbol{\phi}_{\text{b}}^{\text{az}} = \text{arctan2}([\boldsymbol{R}^{\text{T}}(\boldsymbol{p} - \boldsymbol{p}_{\text{RIS}})]_2, [\boldsymbol{R}^{\text{T}}(\boldsymbol{p} - \boldsymbol{p}_{\text{RIS}})]_1), \tag{55}$$

$$\boldsymbol{\phi}_{\text{b}}^{\text{el}} = \arccos\left(\frac{[\boldsymbol{R}^{\text{T}}(\boldsymbol{p} - \boldsymbol{p}_{\text{RIS}})]_3}{\| \boldsymbol{p} - \boldsymbol{p}_{\text{RIS}} \|} \right), \tag{56}$$

where $\Delta_{\text{clk}} \in \mathbb{R}$ is the user's clock bias, c is the speed of light, $\boldsymbol{R} \in \mathbb{C}^{3 \times 3}$ is the rotation matrix defining the RIS's orientation (i.e., $\boldsymbol{R}^{\text{T}} z$ maps z from the global to the local RIS coordinate system), and $[z]_n$ is the nth entry of z. Signal amplitudes may also be used in localization [42], but that is not explored here.

Without an RIS, estimating $\boldsymbol{p}$ from (50) is impossible since the observation yields only $L_d - 1$ TDOA measurements $\{\tau_d^l - \tau_d^1 : l = 2,\ldots,L_d\}$, while there are $3L_d$ unknown geometric parameters: the user location $\boldsymbol{p}$ and locations of the $L_d - 1$ SPs $\boldsymbol{p}_{\text{SP},l}$ (after the removal of the clock bias). However, we will show that adding a single RIS to the setup is sufficient to make the problem identifiable in terms of $\boldsymbol{p}$, though not $\boldsymbol{p}_{\text{SP},l}$. In particular, we will see that the RIS acts as an additional synchronized BS with a phased array. We will describe the localization subproblems in detail: design (offline RIS placement and online RIS configuration), channel parameter estimation (determining $\{\tau_{\text{RIS}}, \boldsymbol{\phi}_b, \tau_d^l : l = 1,\ldots,L_d\}$), localization and synchronization (determining $\boldsymbol{p}$ and Δ_{clk}), and sensing (determining $\{\boldsymbol{p}_{\text{SP},l} : l = 2,\ldots,L_d\}$).

RIS configuration encoding

In localization, propagation paths with similar geometric parameters (angles and delays) will not be resolved when two conditions are met: 1) the delays and angles are similar, and 2) they are correlated. Nonresolved paths can lead to large biases in the estimates of angles and delays. Making the RIS configuration $\bar{\boldsymbol{\omega}}_{\boldsymbol{\theta}}$ time varying provides new dimensions to make paths resolvable. This can be achieved across T transmission blocks as follows. We use $Q \ll T$ RIS configurations $\bar{\boldsymbol{\omega}}_{\boldsymbol{\theta}_1},\ldots,\bar{\boldsymbol{\omega}}_{\boldsymbol{\theta}_Q}$ and associate a unique code (e.g., a column from a DFT matrix) $\boldsymbol{c} = [c_1,\ldots,c_{T/Q}]^{\text{T}} \in \mathbb{C}^{T/Q}, |c_n| = 1$, with a temporal balance property $\boldsymbol{c}^{\text{T}}\mathbf{1} = 0$. The actual RIS configuration is $c_t \bar{\boldsymbol{\omega}}_{\boldsymbol{\theta}_i}$. The switching is done in silent intervals between OFDM blocks to avoid modulating the reflected signals to other bands.

The received signal when using the ith configuration is

$$\begin{aligned}\bar{\boldsymbol{z}}^{(i)}[t] = {} & \sum_{l=1}^{L_d} g^l \boldsymbol{d}(\tau_d^l) \odot \bar{\boldsymbol{x}} + c_t g_{\text{RIS}} \boldsymbol{b}^{\text{T}}(\boldsymbol{\phi}_b) \bar{\boldsymbol{\omega}}_{\boldsymbol{\theta}_i} (\boldsymbol{d}(\tau_{\text{RIS}}) \odot \bar{\boldsymbol{x}}) \\ & + \boldsymbol{w}^{(i)}[t], \quad t = 1,\ldots,\frac{T}{Q},\end{aligned} \tag{57}$$

where we use the same range of time indices for all configurations and separate them using the index i. The observations are grouped as $\boldsymbol{Z}^{(i)} = [\bar{\boldsymbol{z}}^{(i)}[1],\ldots,\bar{\boldsymbol{z}}^{(i)}[T/Q]]$, from which we can compute an observation of the uncontrollable channel as $\hat{\boldsymbol{z}}^{(0)} = \Sigma_{i=1}^{Q} \boldsymbol{Z}^{(i)}\mathbf{1}$ (with processing gain T) and of the ith configuration of the controlled channel as $\hat{\boldsymbol{z}}^{(i)} = \boldsymbol{Z}^{(i)}\boldsymbol{c}^*$ (with processing gain T/Q). This principle significantly reduces the complexity and storage at the RIS and is easy to generalize to a multi-RIS setup.

RIS design for localization and sensing

We want to design an RIS-enabled localization system in a deployment region $\mathcal{R} \subset \mathbb{R}^3$. We rely on Fisher information theory (as developed for wideband localization in [35], which we use as a basis in this article) for offline and online design. We denote the unknown channel parameters as

$$\boldsymbol{\zeta} = [\tau_d^1, \tau_{\text{RIS}}, \boldsymbol{\phi}_b^{\text{T}}, \boldsymbol{\tau}_{l>1}^{\text{T}}, \boldsymbol{g}^{\text{T}}, g_{\text{RIS}}]^{\text{T}}, \tag{58}$$

where $\boldsymbol{\tau}_{l>1} = [\tau_d^2, \tau_d^3,\ldots,\tau_d^{L_d}]^{\text{T}}$ and $\boldsymbol{g} = [g^1, g^2,\ldots,g^{L_d}]^{\text{T}}$. The design parameter vector $\boldsymbol{\sigma}$ accounts for the placement and configuration of the RIS and is selected from a set $\mathcal{S}$. The Fisher information matrix (FIM) can then be defined as

$$\boldsymbol{J}(\boldsymbol{\zeta} | \boldsymbol{\sigma}) = \frac{2}{N_0} \sum_{t=1}^{T} \Re\{(\nabla_{\boldsymbol{\zeta}} \boldsymbol{\mu}[t])^{\text{H}} \nabla_{\boldsymbol{\zeta}} \boldsymbol{\mu}[t]\}, \tag{59}$$

where $\boldsymbol{\mu}[t] = \bar{z}[t] - \bar{\boldsymbol{w}}[t]$ is the noise-free observation, $\nabla_{\boldsymbol{\zeta}} \boldsymbol{\mu}[t] \in \mathbb{C}^{K \times (3L_d + 5)}$ denotes the gradient, and $\Re\{\cdot\}$ returns the real part of its argument. The FIM satisfies the fundamental Fisher information inequality $\boldsymbol{J}^{-1}(\boldsymbol{\zeta} | \boldsymbol{\sigma}) \preceq \mathbb{E}\{(\boldsymbol{\zeta} - \hat{\boldsymbol{\zeta}})(\boldsymbol{\zeta} - \hat{\boldsymbol{\zeta}})^{\text{T}}\}$ (in the positive semidefinite sense), under certain technical conditions, for any unbiased estimator $\hat{\boldsymbol{\zeta}}$ of the channel parameters.

We define a corresponding parameter vector in the location domain $\tilde{\boldsymbol{\zeta}} = [\boldsymbol{p}, \Delta_{\text{clk}}, \boldsymbol{\tau}_{l>1}^{\text{T}}, \boldsymbol{g}^{\text{T}}, g_{\text{RIS}}]^{\text{T}}$ and associated Jacobian $\mathbf{Y} = \nabla_{\tilde{\zeta}} \boldsymbol{\zeta}$ so that $J(\tilde{\boldsymbol{\zeta}} | \boldsymbol{\sigma}) = \mathbf{Y}^{\text{T}} \boldsymbol{J}(\tilde{\boldsymbol{\zeta}} | \boldsymbol{\sigma}) \mathbf{Y}$. From $\boldsymbol{J}(\tilde{\boldsymbol{\zeta}} | \boldsymbol{\sigma})$, we can finally compute the FIM of the user location using Schur's complement: we partition $\boldsymbol{J}(\tilde{\boldsymbol{\zeta}} | \boldsymbol{\sigma}) = [\boldsymbol{A}, \boldsymbol{B}; \boldsymbol{B}^{\text{T}}, \boldsymbol{C}]$, where $\boldsymbol{A} \in \mathbb{R}^{3 \times 3}$ so that $\boldsymbol{J}(\boldsymbol{p} | \boldsymbol{\sigma}) = \boldsymbol{A} - \boldsymbol{B}\boldsymbol{C}^{-1}\boldsymbol{B}^{\text{T}}$. When $\boldsymbol{J}(\boldsymbol{p} | \boldsymbol{\sigma})$ is invertible, we say that the location is identifiable with $\boldsymbol{J}^{-1}(\boldsymbol{p} | \boldsymbol{\sigma}) \preceq \mathbb{E}\{(\boldsymbol{p} - \hat{\boldsymbol{p}})(\boldsymbol{p} - \hat{\boldsymbol{p}})^{\text{T}}\}$. Since the FIM is a matrix, it is inconvenient as a design metric. However, the squared position error bound (SPEB) is a meaningful scalar metric (measured in square meters):

$$\mathrm{SPEB}(\boldsymbol{p}\,|\,\boldsymbol{\sigma}) = \mathrm{trace}(\boldsymbol{J}^{-1}(\boldsymbol{p}\,|\,\boldsymbol{\sigma})) \leq \mathbb{E}\{\|\boldsymbol{p}-\hat{\boldsymbol{p}}\|^2\}. \tag{60}$$

Offline design for optimized coverage

A reasonable criterion for the offline design phase is to provide uniform coverage or maximize the fraction of the deployment region with a low SPEB. The latter can be expressed as

$$\underset{\boldsymbol{\sigma}\in\mathcal{S}}{\mathrm{maximize}}\,\frac{1}{|\mathcal{R}|}\int_{\mathcal{R}}\mathbb{I}\{\mathrm{SPEB}(\boldsymbol{p}\,|\,\boldsymbol{\sigma})\leq\varepsilon^2\}\mathrm{d}\boldsymbol{p}, \tag{61}$$

where $\mathbb{I}$ is an indicator function, $|\mathcal{R}|$ is the size of the deployment region, and ε is a required accuracy (e.g., 1 m). Solving for $\boldsymbol{\sigma}$ leads to the optimal placement of the RIS. The problem (61) can be solved by an exhaustive search across a finite set $\mathcal{S}$, ignoring the uncontrollable channel, except for the LOS path, and using random RIS configurations $\bar{\boldsymbol{\omega}}_{\boldsymbol{\theta}_i}$.

Online design for optimized localization performance

During the online design phase, we possibly have a priori information about the location of the users and origins of the uncontrollable channel. The online problem to minimize the worst-case localization performance is then of the form

$$\underset{\boldsymbol{\sigma}\in\mathcal{S}}{\mathrm{minimize}}\,\max_{\boldsymbol{p}}\,\mathrm{SPEB}(\boldsymbol{p}\,|\,\boldsymbol{\sigma}), \tag{62}$$

where $\boldsymbol{\sigma}$ includes the RIS configuration $\bar{\boldsymbol{\omega}}_{\boldsymbol{\theta}}$. The inner maximization $\max_{\boldsymbol{p}}$ is across the high-probability region of the user location. This problem can be rewritten as

$$\underset{\boldsymbol{\sigma}\in\mathcal{S},\boldsymbol{u}}{\mathrm{minimize}}\,\boldsymbol{u}^{\mathrm{T}}\boldsymbol{1}\ \text{subject to}\begin{bmatrix}\boldsymbol{J}(\tilde{\boldsymbol{\zeta}}\,|\,\boldsymbol{\sigma}) & \boldsymbol{e}_k\\ \boldsymbol{e}_k^T & u_k\end{bmatrix}\succeq\boldsymbol{0},\ k=1,2,3,\ \forall\tilde{\boldsymbol{\zeta}}, \tag{63}$$

where $\boldsymbol{e}_k$ is a vector of zeros, except for a one in the kth entry, and constraints are added for each probable value of $\tilde{\boldsymbol{\zeta}}$. The problem (63) is convex when the variable $\boldsymbol{\sigma}$ appears linearly in $J(\tilde{\zeta}\,|\,\boldsymbol{\sigma})$. The designs that minimize the SPEB are generally different from those that maximize communication-centric metrics, such as the capacity: though both have better performance at a higher SNR, the localization accuracy also depends on the geometry and ability to separate, rather than align, signals from different paths.

Algorithms for estimation, localization, and sensing

The algorithmic design depends on the underlying channel estimation method and specific scenario. The algorithms can be Bayesian (i.e., providing a characterization of the distribution of the user and SP locations) and non-Bayesian (providing only a point estimate). A complete overview of such methods is beyond the scope of this article. Instead, we focus on single-antenna transmitters/receivers defined in (50).

Algorithms for channel parameter estimation

The controllable and uncontrollable channels can be separated using the balanced code described in (57). We obtain the following observation of the uncontrollable channel:

$$\hat{\boldsymbol{z}}^{(0)} = \sum_{i=1}^{Q}\boldsymbol{Z}^{(i)}\boldsymbol{1} = T\sum_{l=1}^{L_d}g^l\boldsymbol{d}(\tau_d^l)\odot\bar{\boldsymbol{x}} + \sum_{t=1}^{T}\sum_{i=1}^{Q}\boldsymbol{w}^{(i)}[t]. \tag{64}$$

Similarly, for the ith configuration of the controllable channel ($i\in\{1,\ldots,Q\}$), we observe that

$$\hat{\boldsymbol{z}}^{(i)} = \boldsymbol{Z}^{(i)}\boldsymbol{c}^* = \frac{T}{Q}g_{\mathrm{RIS}}\boldsymbol{b}^{\mathrm{T}}(\boldsymbol{\phi}_b)\bar{\boldsymbol{\omega}}_{\boldsymbol{\theta}_i}(\boldsymbol{d}(\tau_{\mathrm{RIS}})\odot\bar{\boldsymbol{x}}) + \sum_{t=1}^{T}\boldsymbol{w}^{(i)}[t]c_t^*. \tag{65}$$

The estimation of the uncontrollable channel can be performed using any standard channel approximation technique, e.g., compressive sensing [43]. The approximation of the controllable channel involves only a single path (note that multibounce reflections are very weak and hard to detect) and can be performed using approaches from multiantenna channel estimation [44].

Algorithms for localization and sensing

After channel estimation, the interface toward localization and sensing is via the approximated geometric channel parameters, say, $\{\hat{\tau}_d^l : l=1,\ldots,L_d\}$, $\hat{\tau}_{\mathrm{RIS}}$, and $\hat{\boldsymbol{\phi}}_b$. In the absence of a priori information, localization and sensing are usually performed by determining an initial guess based on the geometric relations and a refinement based on the likelihood function, which itself depends on the underlying channel estimation method, as in the following:

- *Localization*: Assuming the LOS delay can be identified (e.g., from the large path power), (52) and (54) lead to a TDOA measurement, which defines a hyperbola with respect to the user position $\boldsymbol{p}$,

  $$(\hat{\tau}_{\mathrm{RIS}}-\hat{\tau}_d^1)c \approx \|\boldsymbol{p}-\boldsymbol{p}_{\mathrm{RIS}}\| + \|\boldsymbol{p}_{\mathrm{BS}}-\boldsymbol{p}_{\mathrm{RIS}}\| - \|\boldsymbol{p}-\boldsymbol{p}_{\mathrm{BS}}\|, \tag{66}$$

  while measurements of the AOD in (55) and (56) determine a line from the RIS with direction

  $$\boldsymbol{k}(\hat{\boldsymbol{\phi}}_b) \approx \frac{\boldsymbol{R}^{\mathrm{T}}(\boldsymbol{p}-\boldsymbol{p}_{\mathrm{RIS}})}{\|\boldsymbol{R}^{\mathrm{T}}(\boldsymbol{p}-\boldsymbol{p}_{\mathrm{RIS}})\|}. \tag{67}$$

  The intersection of the hyperbola with the line determines the user location, say, $\hat{\boldsymbol{p}}$. An example is provided in Figure 8. Substituting $\hat{\boldsymbol{p}}$ back into (52) provides us with an estimate of the clock bias, say, $\hat{\Delta}_{\mathrm{clk}}$. We note that in the presence of two RISs, the delay measurement is not needed, opening a path for accurate localization across narrowband channels. These estimates can be refined with gradient descent on the likelihood function.
- *Sensing*: After the user location is determined, the sources of the uncontrollable channel are constrained by

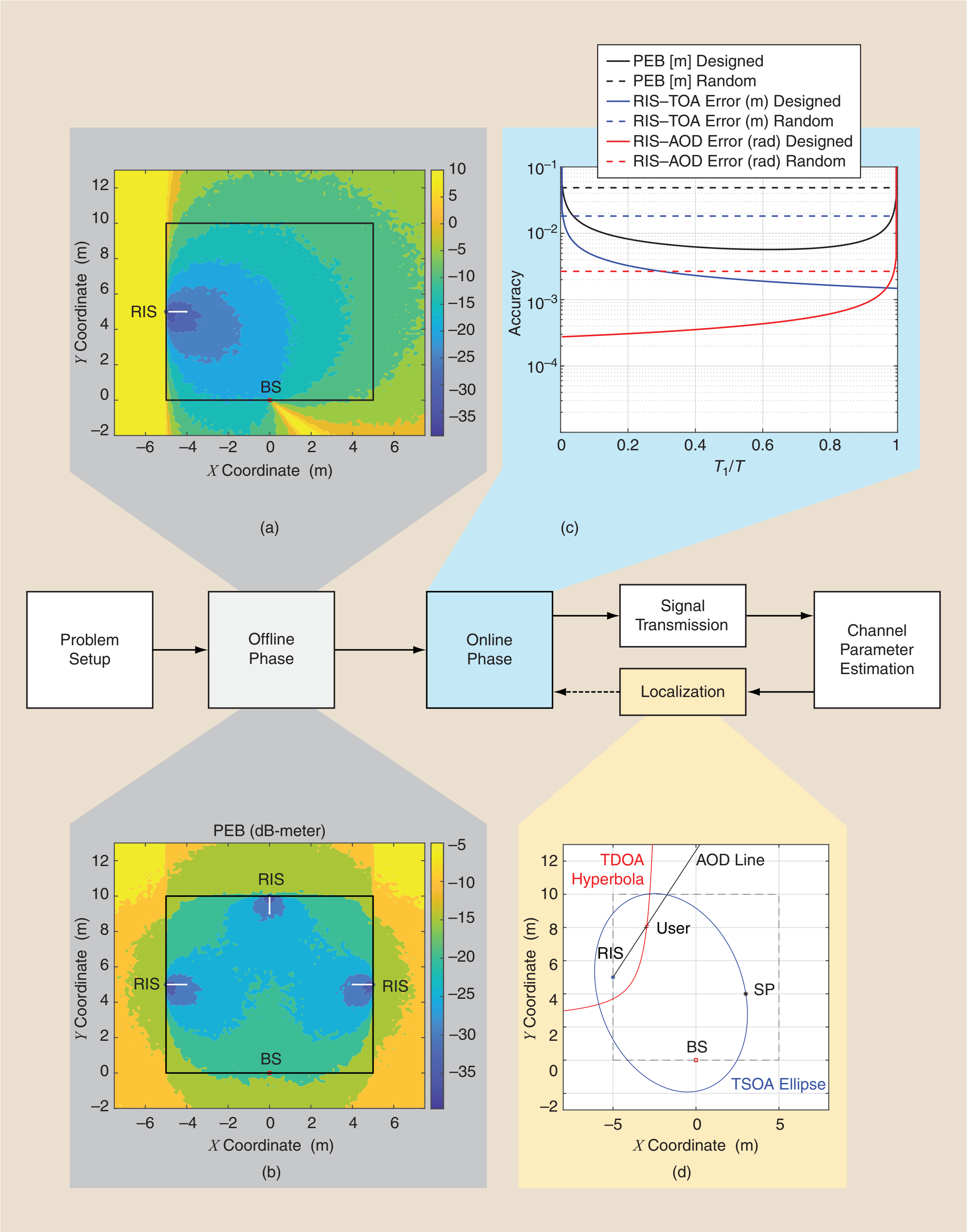

FIGURE 8. The localization (and sensing) problem is solved in a sequence of steps, starting from the problem setup, then proceeding with the offline and online phases, and progressing to the physical transmission, estimation, and localization. The online phase and localization can interact. (a) and (b) The PEB (in decibel-meters) through space for one or three RISs, respectively. The white lines show the normals to the RIS surfaces. (c) The online design for a specific location as a function of the fraction T_1/T of the configurations that maximizes the SNR among the total number of configurations. (d) The localization output based on the LOS and controllable channel. The SP can be constrained to be on an ellipse. TSOA: time-sum-of-arrival.

$$(\hat{\tau}_d^l - \hat{\tau}_d^1)c + \| \hat{\boldsymbol{p}} - \boldsymbol{p}_{\text{BS}} \| \approx \| \hat{\boldsymbol{p}} - \boldsymbol{p}_{\text{SP},l} \| \\ + \| \boldsymbol{p}_{\text{BS}} - \boldsymbol{p}_{\text{SP},l} \|, \quad l > 1. \tag{68}$$

The right-hand side can be interpreted as a time-sum-of-arrival (TSOA), which determines an ellipse with the BS and estimated user location as focal points. Since the controllable channel from the RIS is not dependent on the uncontrollable channel, the RIS does not directly improve sensing but indirectly contributes through better localization accuracy. Note that when there is detectable multibounce multipath (the BS to the RIS to the SP to the user), the AOD from the RIS to the SP can also be inferred, enabling the unique localization of each SP.

Indoor localization example

We will now exemplify the localization in a 2D scenario, where the elevation angle ϕ_b^{el} is removed from the set of unknown parameters to simplify the exposition. The methodology is summarized as a block diagram in Figure 8, and we describe the main blocks. Following the scenario in Figure 7, we consider a $10 \text{ m} \times 10 \text{ m}$ indoor environment with the BS in the middle of a wall at location $\boldsymbol{p}_{\text{BS}} = [0, 0]^{\text{T}}$. An RIS can be placed at the center of each of the three remaining walls. The BS has an antenna that is omnidirectional in the azimuth plane and operates at a carrier frequency of $f_c = 28 \text{ GHz}$ with 400 MHz of bandwidth, using $K = 3{,}000$ subcarriers and a transmission power of 20 decibel milliwatts (dBm). The RIS consists of $N = 64$ elements deployed along a line with $\lambda/5$ spacing (e.g., the total size is about 14 cm) and unity-per-element gain $G(\phi^{\text{az}}) = 1$ for $|\phi^{az}| \leq \pi/2$ and $G(\phi^{\text{az}}) = 0$ elsewhere. The noise power spectral density is $N_0 = -174 \text{ dBm/Hz}$. We use $Q = 8$ RIS configurations and $T = 256$ transmission blocks. The pilot symbols have a constant modulus. We generate

$$g^1 = \frac{\lambda}{4\pi \| \boldsymbol{p} - \boldsymbol{p}_{\text{BS}} \|} e^{\text{j}\psi^1}, \tag{69}$$

$$g^l = \frac{\lambda \sqrt{\sigma_{\text{RCS}}}}{(4\pi)^{3/2}} \frac{1}{\| \boldsymbol{p} - \boldsymbol{p}_{\text{SP},l} \|} \frac{1}{\| \boldsymbol{p}_{\text{SP},l} - \boldsymbol{p}_{\text{BS}} \|} e^{\text{j}\psi^l}, \quad l > 1 \tag{70}$$

$$g_{\text{RIS}} = \sqrt{G(\phi_a^{\text{az}}) G(\phi_b^{\text{az}})} \frac{\left(\frac{\lambda}{5}\right)^2}{4\pi} \frac{1}{\| \boldsymbol{p}_{\text{RIS}} - \boldsymbol{p}_{\text{BS}} \|} \frac{1}{\| \boldsymbol{p}_{\text{RIS}} - \boldsymbol{p} \|} e^{\text{j}\psi_{\text{RIS}}}, \tag{71}$$

where $\psi^l, \psi_{\text{RIS}}$ are independently and uniformly distributed in $[0, 2\pi)$ while σ_{RCS} is the radar cross section (RCS) of the SP, expressed in square meters.

FIM analysis

It is instructive to investigate $\boldsymbol{J}(\boldsymbol{p} | \boldsymbol{\sigma})$ deeper for the case without uncontrollable multipath (only an LOS) and a single RIS. Using RIS configurations with temporal balance and balanced power allocation across subcarriers and an RIS phase reference in the center of the RIS, the FIM of the geometric parameters $[\tau_d^1, \tau_{\text{RIS}}, \phi_b^{\text{az}}]^{\text{T}}$ is a diagonal matrix with entries (see [35, eqs. (16) and (17)] and [45, eq. (4)])

$$J(\tau_d^1) = \frac{2 |g^1|^2}{N_0} T B_{\text{eff}}^2, \tag{72}$$

$$J(\tau_{\text{RIS}}) = \frac{2 | g_{\text{RIS}} |^2 \| \bar{\boldsymbol{x}} \|^2}{N_0} \frac{T}{Q} B_{\text{eff}}^2 \sum_{i=1}^{Q} | \boldsymbol{b}^{\text{T}}(\phi_b^{\text{az}}) \bar{\boldsymbol{\omega}}_{\boldsymbol{\theta}_i} |^2, \tag{73}$$

$$J(\phi_b^{\text{az}}) = \frac{2 | g_{\text{RIS}} |^2 \| \bar{\boldsymbol{x}} \|^2}{N_0} \frac{T}{Q} \\ \cdot \left(\sum_{i=1}^{Q} \left| \dot{\boldsymbol{b}}^{\text{T}}(\phi_b^{\text{az}}) \bar{\boldsymbol{\omega}}_{\boldsymbol{\theta}_i} \right|^2 - \frac{\left| \sum_{i=1}^{Q} (\boldsymbol{b}^{\text{T}}(\phi_b^{\text{az}}) \bar{\boldsymbol{\omega}}_{\boldsymbol{\theta}_i}) \left(\dot{\boldsymbol{b}}^{\text{T}}(\phi_b^{\text{az}}) \bar{\boldsymbol{\omega}}_{\boldsymbol{\theta}_i} \right)^* \right|^2}{\sum_{i=1}^{Q} | \boldsymbol{b}^{\text{T}}(\phi_b^{\text{az}}) \bar{\boldsymbol{\omega}}_{\boldsymbol{\theta}_i} |^2} \right), \tag{74}$$

where $B_{\text{eff}}^2 = \Sigma_{k=1}^{K} (2\pi k \Delta_f)^2 | \bar{x}_k |^2$ and $\dot{\boldsymbol{b}}(\phi_b^{\text{az}})$ denotes the derivative of $\boldsymbol{b}(\phi_b^{\text{az}})$ [defined in (51)] with respect to ϕ_b^{az}. Based on the Jacobian, it can be verified that the FIM becomes

$$\boldsymbol{J}(\boldsymbol{p} | \boldsymbol{\sigma}) = \frac{1}{c^2} \frac{J(\tau_d^1) J(\tau_{\text{RIS}})}{J(\tau_d^1) + J(\tau_{\text{RIS}})} (\boldsymbol{u}_{\text{BS}} - \boldsymbol{u}_{\text{RIS}})(\boldsymbol{u}_{\text{BS}} - \boldsymbol{u}_{\text{RIS}})^{\text{T}} \\ + J(\phi_b^{\text{az}}) \frac{\Xi \boldsymbol{u}_{\text{RIS}} \boldsymbol{u}_{\text{RIS}}^{\text{T}} \Xi^{\text{T}}}{\| \boldsymbol{p}_{\text{RIS}} - \boldsymbol{p} \|^2}, \tag{75}$$

where $\Xi = [0, -1; +1, 0]$ is a rotation matrix across $\pi/2$, $\boldsymbol{u}_{\text{BS}}$ is a unit vector from the BS to the user, and $\boldsymbol{u}_{\text{RIS}}$ a unit vector from the RIS to the user. The expression (75) shows that with aid of the RIS, we obtain two fundamental directions of Fisher information: 1) $\boldsymbol{u}_{\text{BS}} - \boldsymbol{u}_{\text{RIS}}$, with an intensity (as defined in [35]) that depends on the TOA accuracy of the LOS and RIS path, and 2) $\boldsymbol{u}_{\text{RIS}}$, with an intensity reduced with the distance.

This FIM analysis provides contradictory design requirements: for optimal TOA estimation, we should maximize the SNR and set $\bar{\boldsymbol{\omega}}_{\boldsymbol{\theta}_i} = \boldsymbol{b}^*(\phi_b^{\text{az}})$ for all i. This is equivalent to the solution found in (30) that maximizes capacity but leads to $J(\phi_b^{\text{az}}) = 0$, meaning that the AOD cannot be estimated. On the other hand, for optimal AOD estimation, (74) indicates that the RIS configurations $\bar{\boldsymbol{\omega}}_{\boldsymbol{\theta}_i}$ should be a combination of $\boldsymbol{b}^*(\phi_b^{\text{az}})$ from (51) and its derivative $\dot{\boldsymbol{b}}(\phi_b^{\text{az}})$. Hence, a natural compromise is to configure the RIS using $\bar{\boldsymbol{\omega}}_{\boldsymbol{\theta}_i} = \boldsymbol{b}^*(\phi_b^{\text{az}})$ for a fraction of the available transmissions and set $\bar{\boldsymbol{\omega}}_{\boldsymbol{\theta}_i} \approx \dot{\boldsymbol{b}}^*(\phi_b^{\text{az}})$ for the remaining transmissions (which involves approximating the derivative beam to be generated by the RIS so that $| [\bar{\boldsymbol{\omega}}_{\boldsymbol{\theta}_i}]_n | = 1$). By optimizing the fraction, the two terms in (75) can be balanced. The RIS essentially behaves like an additional synchronized BS equipped with a phased array.

Offline design

We first consider five alternative designs: no RIS, an RIS on the left wall, an RIS on the front wall (facing the BS), an RIS on the right wall, and three RISs (one on each remaining wall, using orthogonal temporally balanced codes). Random RIS phase configurations are assumed. Setting the required accuracy to $\varepsilon = 0.1$ m in (61), the fraction of the locations that have a sufficiently low PEB is zero (no RIS), 0.35 (the left RIS), 0.45 (the facing RIS), 0.35 (the right RIS), and 0.99 (the three RISs). This shows that it is better to put the RIS on the wall facing the RIS (despite a larger propagation loss) and that using three RISs can provide uniform coverage in the deployment region.

To gain further insight, Figure 8(a) and (b) show a contour plot of $\mathrm{PEB}(\boldsymbol{x} \mid \boldsymbol{\sigma}) = \sqrt{\mathrm{SPEB}(\boldsymbol{x} \mid \boldsymbol{\sigma})}$ for two of the configurations $\boldsymbol{\sigma}$ (the RIS on the left wall and the three RISs). For visualization purposes, the PEB is expressed in decibel-meters [i.e., $10\log_{10}(\mathrm{PEB})$], where 0 dB-meter means a 1-m uncertainty, -10 dB-meter is a 0.1-m uncertainty, and so on. We see that when an RIS is placed on the left wall, a low PEB is achieved only very close to the RIS, especially in the lower part of the room, closer to the BS. Along the line between the BS and RIS, behind the BS, the PEB tends to infinity since the unit vector from the BS to the user $\boldsymbol{u}_{\mathrm{BS}}$ is parallel to the unit vector from the RIS to the user $\boldsymbol{u}_{\mathrm{RIS}}$, leading to $\boldsymbol{u}_{\mathrm{BS}} - \boldsymbol{u}_{\mathrm{RIS}} = \boldsymbol{0}$ in (75), so the TDOA measurement yields no information. Behind the RIS, the PEB is also infinite due to the zero per-element gain $G(\phi^{\mathrm{az}})$. On the other hand, with three RISs, we can obtain acceptable performance throughout the deployment region.

Online design

We now use a single RIS on the left wall [see Figure 8(a)] and a user at $\boldsymbol{p} = [-3, 8]^{\mathrm{T}}$. We aim to optimize the RIS configuration for this location and consider the following alternatives (which describe the set $\mathcal{S}$ of design variables): 1) set the RIS configurations $\bar{\boldsymbol{\omega}}_{\boldsymbol{\theta}_i}$ to be random, $i = 1, \ldots, 8$, with each configuration used 32 times, and 2) in the $T = 256$ transmissions, use T_1 times the direct beam configuration $\bar{\boldsymbol{\omega}}_{\boldsymbol{\theta}_i} = \boldsymbol{b}^*(\phi_b^{\mathrm{az}})$ and $T - T_1$ times the approximation of the derivative beam configuration $\bar{\boldsymbol{\omega}}_{\boldsymbol{\theta}_i} \approx \dot{\boldsymbol{b}}^*(\phi_b^{\mathrm{az}})$. In Figure 8(c), we evaluate, as a function of T_1/T, the $\mathrm{PEB}(\boldsymbol{p} \mid \boldsymbol{\sigma})$, error standard deviation of $c\tau_{\mathrm{RIS}}$, $c\sqrt{J^{-1}(\tau_{\mathrm{RIS}})}$, and error standard deviation of ϕ_b^{az}, given by $\sqrt{J^{-1}(\phi_b^{\mathrm{az}})}$.

We recall that $T_1 = T$ is optimal in terms of the SNR and TOA estimation accuracy. From a localization perspective, the best performance is achieved when $T_1/T \approx 0.63$, while for $T_1 = 0$ and $T_1 = T$, the PEB diverges. This behavior can be explained by inspecting the TOA and AOD: a large T_1 leads to a high SNR and maximizes $J(\tau_{\mathrm{RIS}})$, so the best TOA estimation from the RIS is achieved when only $\bar{\boldsymbol{\omega}}_{\boldsymbol{\theta}_i} = \boldsymbol{b}^*(\phi_b^{\mathrm{az}})$ is used. However, in that case, $J(\phi_b^{\mathrm{az}}) \to 0$ so that the measurement does not provide any information about the AOD from the RIS. While not obvious from the figure, when only $\bar{\boldsymbol{\omega}}_{\boldsymbol{\theta}_i} \approx \dot{\boldsymbol{b}}^*(\phi_b^{\mathrm{az}})$ is sent, $J(\tau_{\mathrm{RIS}}) = J(\phi_b^{\mathrm{az}}) = 0$ since $\boldsymbol{b}^{\mathrm{T}}(\phi_b^{\mathrm{az}})\dot{\boldsymbol{b}}^*(\phi_b^{\mathrm{az}}) = 0$. The random configurations (though providing information when there is no prior on the user location) lead to a worse PEB than the optimally designed arrangements.

Localization and sensing

As a final example, we again use a single RIS on the left wall, a user at $\boldsymbol{p} = [-3, 8]^{\mathrm{T}}$, and an SP at location $\boldsymbol{p}_{\mathrm{SP}} = [3, 4]^{\mathrm{T}}$ with an RCS of $\sigma_{\mathrm{RCS}} = 1\ \mathrm{m}^2$. To estimate the delays of the uncontrollable channel, we apply a DFT to (64) and determine the peaks. These can then be converted to $\hat{\tau}_d^1$ and $\hat{\tau}_d^2$. To estimate the TOA and AOD from the controllable channel, we use (65) and perform a 2D search across $[\tau_{\mathrm{RIS}}, \phi_b^{\mathrm{az}}]$ with a substituted estimate of the channel gain. This yields $\hat{\tau}_{\mathrm{RIS}}$ and $\hat{\boldsymbol{\phi}}_b$. Figure 8(d) graphs the locations of the BS, user, RIS, and SP, and it shows the TDOA hyperbola from (66) as well as the AOD bearing line from (67). Their intersection is the estimated location $\hat{\boldsymbol{p}}$. From this estimated location and the TOA of the uncontrollable channel, we obtain a TSOA ellipse (68), near which the SP must lie. Note that from a snapshot, the SP location cannot be determined, but after sufficient movement of the user and appropriate data association, the SP position can be uniquely identified.

Conclusions from RIS-aided localization

An RIS can be seen as a synchronized multiantenna BS with a phased array that can aid localization. Proper RIS placement can provide significant location coverage improvements. The RIS configuration can be tailored to a specific user location but is significantly different than the optimal configuration for communications. This is also reflected by the different simulation setups considered in this article: many RIS elements are required in communication to improve the end-to-end SNR, while localization requires large bandwidths, but an RIS can be small since it is primarily used to add new dimensions to resolve identifiability issues. An increase in the number of RIS elements can enable the use of less bandwidth. While for communication, an RIS provides limited gains when the LOS path is present, for localization, both paths provide useful and necessary information. Moreover, by encoding the RIS configurations with a global code, the controllable and uncontrollable channels can be separated, and multiple noninterfering RISs can be supported. The use of an RIS for sensing is mainly indirect, through the improved estimation of the user location, if the uncontrollable and controllable channels do not interact.

Future model evolution and related signal processing challenges

We elaborate on a few fundamental phenomena that appear when having a large and dense RIS. By refining the models to capture these properties, there are opportunities to develop new signal processing algorithms that push the boundaries of how communication and localization are normally conceived.

Scaling laws and near-field regime

The benefit of classical beamforming from an antenna array is that the SNR grows linearly with the number of antennas N [1]. When maximizing the narrowband capacity, we noticed that the SNR with an RIS instead grows as $N^2\alpha\beta\gamma$ when the N paths have the same propagation loss. The quadratic SNR scaling does not mean that the setup in Figure 1(b) can achieve a higher SNR than in a case where the RIS is replaced by an equal-sized antenna array that is transmitting with the same power. In the latter case, the SNR would be proportional to $N\beta$. To understand the difference, we can factorize the SNR scaling achieved by the RIS as $(N\alpha\gamma) \cdot (N\beta)$.

The first term accounts for the fraction of the transmitter's signal power that is reflected by the RIS, which is a very small number even when N is large since $\alpha < -70$ dB is typical. Hence, the RIS cannot achieve a higher SNR than $N\beta$, but the difference reduces as $1/N$. When comparing an RIS with alternative technologies, it must be physically larger to be competitive [5].

SNR scaling behaviors are extensively studied in signal processing for communication and localization to understand the ultimate performance and obtain intuitive performance approximations for cases with large arrays. Although the asymptotic regime where $N \to \infty$ is commonly studied, practical technologies have operated far from the limit, so it has been unimportant whether the underlying models are asymptotically accurate or not. Since the law of conservation of energy dictates that we cannot receive more power than what was transmitted, the SNR must approach a finite upper limit as $N \to \infty$. The aforementioned SNR scaling was obtained under a far-field assumption: the propagation losses $\alpha_n \beta_n$ are equal for all N RIS elements. However, when the transmitter and receiver are at a distance from the RIS similar to the RIS's width/height, the geometry will make $\alpha_n \beta_n$ widely different between the elements [23]. This scenario is unavoidable as $N \to \infty$ but also occurs in practice when the RIS is 1 m wide and the user is at a similar distance.

The general SNR expressions presented in this tutorial remain valid, and if propagation loss models that capture the radiative near-field properties are utilized, one can derive how the SNR converges to a finite upper limit [23]. More importantly, the near field enables the RIS to focus signals not only in a particular direction but at a certain point in that direction, thereby making a flat RIS better than a flat mirror [5]. This property can also be utilized for improved localization [41]. Since classical array signal processing focuses on the far field, there are great opportunities to develop new algorithms that exploit the unique near-field properties for improved communication and localization.

Channel modeling and sparsity

The system models in this article can be utilized for any LTI channel, but the channel modeling for the RIS is in its infancy, with limited experimental validation. In a multipath environment, different parts of the RIS will observe various linear combinations of the impinging waves, leading to fading variations. The wavelength limits the variability, and, even in rich scattering, there will be correlation between the channel coefficients observed at RIS elements that are within a few wavelengths [21]. This fundamental property has several impacts on RIS operation. The resulting spatial sparsity can be exploited to simplify channel estimation. It also enables an RIS to reflect multiple signals to different locations simultaneously, thereby enabling communication and localization with multiple users. The modeling of how an RIS interacts with interference from other systems and electromagnetic noise remains open. There are signal processing research challenges in system modeling, algorithmic design, and optimization.

Nonlinear RIS operation

This article focuses on applications where the RIS has a (piecewise) constant configuration, so the RIS can be modeled as a linear filter. We also explained how LTV system theory can be used in the case where the RIS is tuned to mitigate the Doppler effect caused by mobility. A different option is to vary the RIS configuration continuously during the transmission of a signal block to modulate the transmitted signal before it is reradiated [46]. This effectively creates a nonlinear end-to-end channel where the received signal contains a wider range of frequencies than the transmitted signal. The key applications remain to be discovered, but it is clear that signal processing provides the right tools for analysis and optimization.

Mutual coupling

A model assumption that was made in Figure 1(b) is that the N elements act as separate filters that each take a single input. However, when the RIS elements are closely spaced, it is hard to fully isolate them on the substrate material. This leads to mutual coupling, where the impedance of one element is connected with the impedances of neighboring ones. Hence, if the curves in Figure 1 exemplify how an RIS element behaves in isolation, in reality, the frequency response will also depend on the configuration of the nearby elements. The mutual impedance is dependent on the physical properties of the components and can be determined through lengthy full-wave simulations, such as the method of moments, that must be carried out for each configuration. Such an analysis has previously been done for antenna arrays. The special case of canonical minimum-scattering (CMS) antennas [47] enables expressing the mutual impedance as a closed-form function of the distance and orientations of two antennas [48], [49].

The CMS approach, however, does not capture the desired operation of the RIS, as CMS antennas do not facilitate full 2π phase control [50]. In contrast, an RIS made from patch or slot antennas effectively decouples the amplitude and phase of the reflected wave, enabling full 2π phase control. Without proper modeling of the mutual impedance, the tradeoff between complexity and performance as the RIS is densified cannot be evaluated. Therefore, different modeling techniques that do not rely on the CMS assumption have to be developed to capture the behavior of RISs with closely spaced elements.

For conventional antenna arrays, mutual coupling carries drawbacks, such as scan blindness and ohmic losses. Scan blindness is when a wave is fully reflected, and it might be a desirable effect for an RIS. The high ohmic losses of superdirectivity could potentially be utilized to absorb interference as heat. Hence, these effects present themselves as new opportunities that should be reevaluated in the RIS context. A methodology based on circuit theory can be utilized to develop discrete-time RIS system models that capture mutual coupling, but this research is in its infancy. Mutual coupling will have an impact on algorithmic design as well as communication/localization performance. If accurate models are hard to develop, machine learning methods might be useful to address the problem of system identification.

Summary

This article provided a tutorial on the basic system modeling of wireless signaling that involves RISs. This emerging technology can be utilized to increase the capacity of communication systems and accuracy of localization and sensing systems. While the same models underpin both applications, the preferred embodiments differ in terms of bandwidth requirements, RIS dimensions, and optimal configuration. The basic algorithms and properties have been described in this article, but there is a gold mine of open signal processing problems, for example, related to refined models capturing the relevant electromagnetic properties, experimental validation, and more realistic applications. Since RIS technology is often mentioned in 6G research, now is the right time to explore these open issues.

Acknowledgments

We would like to thank Gonzalo Seco-Granados, Kamran Keykhosravi, Özlem Tugfe Demir, and Robin J. Williams for their comments and feedback. This work has been partially supported by the Horizon 2020 Reconfigurable Intelligent Sustainable Environments for 6G Wireless Networks project, under grant 101017011, the German Research Foundation (DFG) under Germany's Excellence Strategy (EXC 2077 at University of Bremen, University Allowance), the Italian Ministry of Education and Research in the framework of the CrossLab Project, and the FFL18-0277 grant from the Swedish Foundation for Strategic Research.

Authors

Emil Björnson (emilbjo@kth.se) received his Ph.D. degree from KTH Royal Institute of Technology in 2011. He is a professor at KTH Royal Institute of Technology, Stockholm, 10044, Sweden. His research interests include multiple-input, multiple-output and reconfigurable intelligent surface-aided communications; radio resource allocation; and energy efficiency. He received the 2018 IEEE Marconi Prize Paper Award, 2019 European Association for Signal Processing Early Career Award, 2019 IEEE Fred W. Ellersick Prize, 2020 Pierre-Simon Laplace Early Career Technical Achievement Award, 2020 Communication Theory Technical Committee Early Achievement Award, and 2021 IEEE Communications Society Radio Communications Committee Early Achievement Award. He is a Fellow of IEEE.

Henk Wymeersch (henkw@chalmers.se) received his Ph.D. degree from Ghent University, Belgium, in 2005. He is a professor of communication systems at Chalmers University of Technology, Göteborg, 41296, Sweden, and a distinguished research associate at Eindhoven University of Technology, Eindhoven, The Netherlands. His research interests include the convergence of communication, localization, and sensing. He was a corecipient of the Best Paper Award and Best Student Paper Award at the 2021 International Conference on Information Fusion.

Bho Matthiesen (matthiesen@uni-bremen.de) received his Ph.D. degree from TU Dresden, Germany, in 2019. He is a research group leader at the University of Bremen Excellence Chair of Petar Popovski, Department of Communications Engineering, University of Bremen, Bremen, 28359, Germany. His research interests include communication theory, wireless communications, and optimization theory. He was a 2020 *IEEE Wireless Communications Letters* Exemplary Reviewer, an invited speaker at the 2nd 6G Wireless Summit 2020, and a publication chair for the 2021 International Symposium on Wireless Communication Systems.

Petar Popovski (petarp@es.aau.dk) received his Ph.D. degree from Aalborg University, Aalborg, 9220, Denmark, where he is a professor heading the section on connectivity. His research interests include wireless communications/networks and communication theory. He authored the book *Wireless Connectivity: An Intuitive and Fundamental Guide*, published by Wiley in 2020; held a European Research Council Consolidator Grant (2015–2020); and is a Villum Investigator. He is an IEEE Communications Society Board of Governors member at large and a Fellow of IEEE.

Luca Sanguinetti (luca.sanguinetti@unipi.it) received his Ph.D. degree in information engineering from the University of Pisa, Pisa, 56125, Italy, in 2005, where he is an associate professor. His research interests include wireless communications and signal processing for communications, with emphasis on multiple antenna technologies. He coauthored two textbooks: *Massive MIMO Networks: Spectral, Energy, and Hardware Efficiency* (2017) and *Foundations of User-Centric Cell-Free Massive MIMO* (2020). He received the 2018 Marconi Prize Paper Award in Wireless Communications.

Elisabeth de Carvalho (edc@es.aau.dk) received her Ph.D. degree in electrical engineering from Telecom ParisTech, France. She is a professor at Aalborg University, Aalborg, 9220, Denmark. Her research interests include signal processing with emphasis on multiple-input, multiple-output communications, and she coauthored the book *A Practical Guide to the MIMO Radio Channel*. She is a member of the IEEE Signal Processing Society (SPS) and SPS Signal Processing for Communications and Networking Technical Committee, and she is vice chair of the IEEE Communications Society Emerging Technology Initiative on Machine Learning for Communications. She is an associate editor of *IEEE Transactions of Wireless Communications* and the coordinator of the European Union Horizon 2020 Innovative Training Network WindMill.

References

[1] B. D. V. Veen and K. M. Buckley, "Beamforming: A versatile approach to spatial filtering," *IEEE ASSP Mag.*, vol. 5, no. 2, pp. 4–24, 1988, doi: 10.1109/53.665.

[2] E. Björnson, L. Sanguinetti, H. Wymeersch, J. Hoydis, and T. L. Marzetta, "Massive MIMO is a reality—What is next? Five promising research directions for antenna arrays," *Digit. Signal Process.*, vol. 94, pp. 3–20, Nov. 2019, doi: 10.1016/j.dsp.2019.06.007.

[3] K. Witrisal *et al.*, "High-accuracy localization for assisted living: 5G systems will turn multipath channels from foe to friend," *IEEE Signal Process. Mag.*, vol. 33, no. 2, pp. 59–70, 2016, doi: 10.1109/MSP.2015.2504328.

[4] O. Tsilipakos *et al*., “Toward intelligent metasurfaces: The progress from globally tunable metasurfaces to software-defined metasurfaces with an embedded network of controllers,” *Adv.Opt. Mater.*, vol. 8, no. 17, p. 2,000,783, 2020, doi: 10.1002/adom.202000783.

[5] E. Björnson, Ö. Özdogan, and E. G. Larsson, “Reconfigurable intelligent surfaces: Three myths and two critical questions,” *IEEE Commun. Mag.*, vol. 58, no. 12, pp. 90–96, 2020, doi: 10.1109/MCOM.001.2000407.

[6] C. Liaskos, S. Nie, A. Tsioliaridou, A. Pitsillides, S. Ioannidis, and I. Akyildiz, “A new wireless communication paradigm through software-controlled metasurfaces,” *IEEE Commun. Mag.*, vol. 56, no. 9, pp. 162–169, 2018, doi: 10.1109/MCOM.2018.1700659.

[7] M. D. Renzo, A. Zappone, M. Debbah, M. S. Alouini, C. Yuen, J. De Rosny, and S. Tretyakov, “Smart radio environments empowered by reconfigurable intelligent surfaces: How it works, state of research, and road ahead,” *IEEE J. Sel. Areas Commun.*, vol. 38, no. 11, pp. 2450–2525, 2020, doi: 10.1109/JSAC.2020.3007211.

[8] H. Wymeersch, J. He, B. Denis, A. Clemente, and M. Juntti, “Radio localization and mapping with reconfigurable intelligent surfaces: Challenges, opportunities, and research directions,” *IEEE Veh. Technol. Mag.*, vol. 15, no. 4, pp. 52–61, 2020, doi: 10.1109/MVT.2020.3023682.

[9] M. D. Renzo *et al*., “Smart radio environments empowered by reconfigurable AI meta-surfaces: An idea whose time has come,” *EURASIP J. Wireless Commun. Netw.*, vol. 2019, May 2019, Art. no. 129.

[10] P. Popovski, *Wireless Connectivity: An Intuitive and Fundamental Guide*. Hoboken, NJ, USA: Wiley, 2020.

[11] Q. He, S. Sun, and L. Zhou, “Tunable/reconfigurable metasurfaces: Physics and applications,” *Research*, vol. 2019, Jul. 2019, Art. no. 1849272.

[12] B. Assouar, B. Liang, Y. Wu, Y. Li, J. C. Cheng, and Y. Jing, “Acoustic metasurfaces,” *Nature Rev. Mater.*, vol. 3, no. 12, pp. 460–472, 2018, doi: 10.1038/s41578-018-0061-4.

[13] Q. Wu, S. Zhang, B. Zheng, C. You, and R. Zhang, “Intelligent reflecting surface-aided wireless communications: A tutorial,” *IEEE Trans. Commun.*, vol. 69, no. 5, pp. 3313–3351, 2021, doi: 10.1109/TCOMM.2021.3051897.

[14] C. Huang, A. Zappone, G. C. Alexandropoulos, M. Debbah, and C. Yuen, “Reconfigurable intelligent surfaces for energy efficiency in wireless communication,” *IEEE Trans. Wireless Commun.*, vol. 18, no. 8, pp. 4157–4170, 2019, doi: 10.1109/TWC.2019.2922609.

[15] J. Huang, *Reflectarray Antenna*. Hoboken, NJ, USA: Wiley, 2005.

[16] P. Nayeri, F. Yang, and A. Z. Elsherbeni, “Beam-scanning reflectarray antennas: A technical overview and state of the art,” *IEEE Antennas Propag. Mag.*, vol. 57, no. 4, pp. 32–47, 2015, doi: 10.1109/MAP.2015.2453883.

[17] B. Zhu, J. Zhao, and Y. Feng, “Active impedance metasurface with full 360° reflection phase tuning,” *Sci. Rep.*, vol. 3, no. 1, 2013, Art. no. 3059.

[18] Ö. Özdogan, E. Björnson, and E. G. Larsson, “Intelligent reflecting surfaces: Physics, propagation, and pathloss modeling,” *IEEE Wireless Commun. Lett.*, vol. 9, no. 5, pp. 581–585, 2020, doi: 10.1109/LWC.2019.2960779.

[19] Q. Wu and R. Zhang, “Towards smart and reconfigurable environment: Intelligent reflecting surface aided wireless network,” *IEEE Commun. Mag.*, vol. 58, no. 1, pp. 106–112, 2020, doi: 10.1109/MCOM.001.1900107.

[20] S. Abeywickrama, R. Zhang, Q. Wu, and C. Yuen, “Intelligent reflecting surface: Practical phase shift model and beamforming optimization,” *IEEE Trans. Commun.*, vol. 68, no. 9, pp. 5849–5863, 2020, doi: 10.1109/TCOMM.2020.3001125.

[21] E. Björnson and L. Sanguinetti, “Rayleigh fading modeling and channel hardening for reconfigurable intelligent surfaces,” *IEEE Wireless Commun. Lett.*, vol. 10, no. 4, pp. 830–834, 2021, doi: 10.1109/LWC.2020.3046107.

[22] M. Di Renzo *et al*., “Reconfigurable intelligent surfaces vs. relaying: Differences, similarities, and performance comparison,” *IEEE Open J. Commun. Soc.*, vol. 1, pp. 798–807, Jun. 2020, doi: 10.1109/OJCOMS.2020.3002955.

[23] E. Björnson and L. Sanguinetti, “Power scaling laws and near-field behaviors of massive MIMO and intelligent reflecting surfaces,” *IEEE Open J. Commun. Soc.*, vol. 1, pp. 1306–1324, Sep. 2020, doi: 10.1109/OJCOMS.2020.3020925.

[24] Q. Wu and R. Zhang, “Intelligent reflecting surface enhanced wireless network via joint active and passive beamforming,” *IEEE Trans. Wireless Commun.*, vol. 18, no. 11, pp. 5394–5409, 2019, doi: 10.1109/TWC.2019.2936025.

[25] B. Matthiesen, E. Björnson, E. de Carvalho, and P. Popovski, “Intelligent reflecting surface operation under predictable receiver mobility: A continuous time propagation model,” *IEEE Wireless Commun. Lett.*, vol. 10, no. 2, pp. 216–220, 2021, doi: 10.1109/LWC.2020.3024781.

[26] E. Basar, “Transmission through large intelligent surfaces: A new frontier in wireless communications,” in *Proc. Eur. Conf. Netw. Commun. (EuCNC)*, 2019, pp. 112–117, doi: 10.1109/EuCNC.2019.8801961.

[27] Q. Wu and R. Zhang, “Beamforming optimization for wireless network aided by intelligent reflecting surface with discrete phase shifts,” *IEEE Trans. Commun.*, vol. 68, no. 3, pp. 1838–1851, 2020, doi: 10.1109/TCOMM.2019.2958916.

[28] R. G. Gallager, *Principles of Digital Communication*. Cambridge, U.K.: Cambridge Univ. Press, 2008.

[29] D. Ramaccia, D. L. Sounas, A. Alù, A. Toscano, and F. Bilotti, “Doppler cloak restores invisibility to objects in relativistic motion,” *Phys. Rev. B*, vol. 95, no. 7, pp. 075113, Feb. 2017, doi: 10.1103/PhysRevB.95.075113.

[30] Y. Yang, B. Zheng, S. Zhang, and R. Zhang, “Intelligent reflecting surface meets OFDM: Protocol design and rate maximization,” *IEEE Trans. Commun.*, vol. 68, no. 7, pp. 4522–4535, 2020, doi: 10.1109/TCOMM.2020.2981458.

[31] B. Zheng and R. Zhang, “Intelligent reflecting surface-enhanced OFDM: Channel estimation and reflection optimization,” *IEEE Wireless Commun. Lett.*, vol. 9, no. 4, pp. 518–522, 2020, doi: 10.1109/LWC.2019.2961357.

[32] S. Lin, B. Zheng, G. C. Alexandropoulos, M. Wen, and F. Chen, “Adaptive transmission for reconfigurable intelligent surface-assisted OFDM wireless communications,” *IEEE J. Sel. Areas Commun.*, vol. 38, no. 11, pp. 2653–2665, 2020, doi: 10.1109/JSAC.2020.3007038.

[33] “Spatial channel model for Multiple Input Multiple Output (MIMO) simulations (Release 16),” 3GPP, Sophia Antipolis, France, TS 25.996, Jul. 2020.

[34] A. Taha, M. Alrabeiah, and A. Alkhateeb, “Enabling large intelligent surfaces with compressive sensing and deep learning,” *IEEE Access*, vol. 9, pp. 44,304–44,321, Mar. 2021, doi: 10.1109/ACCESS.2021.3064073.

[35] Y. Shen and M. Z. Win, “Fundamental limits of wideband localization–part I: A general framework,” *IEEE Trans. Inf. Theory*, vol. 56, no. 10, pp. 4956–4980, 2010, doi: 10.1109/TIT.2010.2060110.

[36] J. A. del Peral-Rosado, R. Raulefs, J. A. López-Salcedo, and G. Seco-Granados, “Survey of cellular mobile radio localization methods: From 1G to 5G,” *IEEE Commun. Surveys Tuts.*, vol. 20, no. 2, pp. 1124–1148, 2017, doi: 10.1109/COMST.2017.2785181.

[37] E. Leitinger, F. Meyer, F. Hlawatsch, K. Witrisal, F. Tufvesson, and M. Z. Win, “A belief propagation algorithm for multipath-based SLAM,” *IEEE Trans. Wireless Commun.*, vol. 18, no. 12, pp. 5613–5629, 2019, doi: 10.1109/TWC.2019.2937781.

[38] R. M. Buehrer, H. Wymeersch, and R. M. Vaghefi, “Collaborative sensor network localization: Algorithms and practical issues,” *Proc. IEEE*, vol. 106, no. 6, pp. 1089–1114, 2018, doi: 10.1109/JPROC.2018.2829439.

[39] Y. Ge, F. Wen, H. Kim, M. Zhu, F. Jiang, S. Kim, L. Svensson, and H. Wymeersch, “5G SLAM using the clustering and assignment approach with diffuse multipath,” *Sensors*, vol. 20, no. 16, p. 4656, 2020, doi: 10.3390/s20164656.

[40] A. Bourdoux *et al*., “6G white paper on localization and sensing,” 2020, arXiv:2006.01779.

[41] A. Elzanaty, A. Guerra, F. Guidi, and M.-S. Alouini, “Reconfigurable intelligent surfaces for localization: Position and orientation error bounds,” *IEEE Trans. Signal Process.*, vol. 69, pp. 5386–5402, Aug. 2021, doi: 10.1109/TSP.2021.3101644.

[42] H. Zhang, H. Zhang, B. Di, K. Bian, Z. Han, and L. Song, “Towards ubiquitous positioning by leveraging reconfigurable intelligent surface,” *IEEE Commun. Lett.*, vol. 25, no. 1, pp. 284–288, 2020, doi: 10.1109/LCOMM.2020.3023130.

[43] K. Venugopal, A. Alkhateeb, N. G. Prelcic, and R. W. Heath, “Channel estimation for hybrid architecture-based wideband millimeter wave systems,” *IEEE J. Sel. Areas Commun.*, vol. 35, no. 9, pp. 1996–2009, 2017, doi: 10.1109/JSAC.2017.2720856.

[44] A. Fascista, A. Coluccia, H. Wymeersch, and G. Seco-Granados, “Millimeter-wave downlink positioning with a single-antenna receiver,” *IEEE Trans. Wireless Commun.*, vol. 18, no. 9, pp. 4479–4490, 2019, doi: 10.1109/TWC.2019.2925618.

[45] N. Garcia, H. Wymeersch, and D. T. M. Slock, “Optimal precoders for tracking the AoD and AoA of a mmWave path,” *IEEE Trans. Signal Process.*, vol. 66, no. 21, pp. 5718–5729, 2018, doi: 10.1109/TSP.2018.2870368.

[46] J. Yuan, E. de Carvalho, R. J. Williams, E. Björnson, and P. Popovski, “Frequency-mixing intelligent reflecting surfaces for nonlinear wireless propagation,” *IEEE Wireless Commun. Lett.*, vol. 10, no. 8, pp. 1672–1676, 2021, doi: 10.1109/LWC.2021.3077085.

[47] W. Wasylkiwskyj and W. K. Kahn, “Theory of mutual coupling among minimum-scattering antennas,” *IEEE Trans. Antennas Propag.*, vol. 18, no. 2, pp. 204–216, 1970, doi: 10.1109/TAP.1970.1139649.

[48] G. Gradoni and M. Di Renzo, “End-to-end mutual coupling aware communication model for reconfigurable intelligent surfaces: An electromagnetic-compliant approach based on mutual impedances,” *IEEE Wireless Commun. Lett.*, vol. 10, no. 5, pp. 938–942, 2021, doi: 10.1109/LWC.2021.3050826.

[49] R. J. Williams, P. Ramírez-Espinosa, E. de Carvalho, and T. L. Marzetta, “Multiuser MIMO with large intelligent surfaces: Communication model and transmit design,” in *Proc. IEEE Int. Conf. Commun.*, 2021, pp. 1–6, doi: 10.1109/ICC42927.2021.9500830.

[50] X. Qian and M. D. Renzo, “Mutual coupling and unit cell aware optimization for reconfigurable intelligent surfaces,” *IEEE Wireless Commun. Lett.*, vol. 10, no. 6, pp. 1183–1187, 2021, doi: 10.1109/LWC.2021.3061449.